remote sensing

Article

A Novel Remote Sensing-Based Modeling Approach for Maize Light Extinction Coefficient Determination

Edson Costa-Filho [1], José L. Chávez [1,*] and Huihui Zhang [2]

[1] Civil and Environmental Engineering Department, Colorado State University, Fort Collins, CO 80523, USA; edscos@colostate.edu

[2] Water Management and Systems Research Unit, Agricultural Research Service, United States Department of Agriculture, Fort Collins, CO 80526, USA; huihui.zhang@usda.gov

* Correspondence: jose.chavez@colostate.edu

Abstract: This study focused on developing a novel semi-empirical model for maize's light extinction coefficient (k_p) by integrating multiple remotely sensed vegetation features from several different remote sensing platforms. The proposed k_p model's performance was independently evaluated using Campbell's (1986) original and simplified k_p approaches. The Limited Irrigation Research Farm (LIRF) in Greeley, Colorado, and the Irrigation Innovation Consortium (IIC) in Fort Collins, Colorado, USA, served as experimental sites for developing and evaluating the novel maize k_p model. Data collection involved multiple remote sensing platforms, including Landsat-8, Sentinel-2, Planet CubeSat, a Multispectral Handheld Radiometer, and an unmanned aerial system (UAS). Ground measurements of leaf area index (LAI) and fractional vegetation canopy cover (f_c) were included. The study evaluated the novel k_p model through a comprehensive analysis using statistical error metrics and Sobol global sensitivity indices to assess the performance and sensitivity of the models developed for predicting maize k_p. Results indicated that the novel k_p model showed strong statistical regression fitting results with a coefficient of determination or R^2 of 0.95. Individual remote sensor analysis confirmed consistent regression calibration results among Landsat-8, Sentinel-2, Planet CubeSat, the MSR, and UAS. A comparison with Campbell's (1986) k_p models reveals a 44% improvement in accuracy. A global sensitivity analysis identified the role of the normalized difference vegetation index (NDVI) as a critical input variable to predict k_p across sensors, emphasizing the model's robustness and potential practical environmental applications. Further research should address sensor-specific variations and expand the k_p model's applicability to a diverse set of environmental and microclimate conditions.

Keywords: environmental biophysics; remote sensing; spatial modeling; gap fraction; canopy architecture; vegetation indices

check for updates

Citation: Costa-Filho, E.; Chávez, J.L.; Zhang, H. A Novel Remote Sensing-Based Modeling Approach for Maize Light Extinction Coefficient Determination. *Remote Sens.* **2024**, *16*, 1012. https://doi.org/10.3390/rs16061012

Academic Editors: Jean-Philippe Gastellu-Etchegorry, Tiangang Yin, Shanshan Wei and Hao Tang

Received: 27 January 2024
Revised: 1 March 2024
Accepted: 4 March 2024
Published: 13 March 2024

1. Introduction

The vegetation growth and biomass development of forest plants and crops are directly related to the capacity of plants to intercept, transmit, and absorb solar energy in the form of incoming photosynthetically active radiation, often known as PAR [1–7]. When characterizing the canopy architecture arrangement of plants, vegetation indices such as the leaf area density (LAD), leaf area index (LAI), and fractional vegetation cover (f_c) provide information on the canopy status regarding the assemblage of above-ground plant elements (leaves, stems, branches, etc.) on a spatio-temporal basis [8]. The LAD index concerns the one-sided green leaf area per unit of canopy volume [9]. The LAI is often defined as the total area occupied by plant leaves per unit area of the ground surface, while f_c is the fraction of surface land occupied by plant elements [10]. The LAI is also defined as the integral of the LAD over canopy height [11].

Canopy architecture variables directly influence environmental biophysics processes associated with crop yield, plant transpiration, and carbon retention [12–14]. Understanding canopy architecture has potential benefits for maximally utilizing commercial plants' or crops' land area, space, and light energy [15]. Also, the canopy architecture arrangement has a vital influence on the dynamics regarding the physical processes of water vapor and carbon exchange within the soil–plant–atmosphere continuum [16–19]. In the field of environmental biophysics, the LAI and f_c are related to each other through the light attenuation (or "canopy gap fraction") theory [20,21].

The light attenuation concept relies on the assumption that as PAR light reaches a vegetation surface, the interactions between the light beam and the number of plant elements (leaves, stem, branches, etc.) cause light to be transmitted, absorbed, or reflected by the plant elements [8]. Thus, the PAR flux above the canopy is reduced as the light beam travels through the canopy towards the ground surface, which constitutes the "canopy gap fraction" (f_{PAR}) between the source of incoming PAR flux above the canopy (φ_o) and the downward short-wave irradiance (light flux) within the canopy (φ_{down}). Several studies indicate that f_{PAR} can be explained and modeled using a decaying exponential function based on the Beer–Lambert spectroscopy law for randomly distributed canopy leaves [22–25], as indicated by Equations (1) and (2):

$$f_{PAR} = \exp\left(-k_p \times \mathrm{LAI}\right) \tag{1}$$

$$f_{PAR} = \varphi_{down}/\varphi_o \tag{2}$$

where φ_{down} and φ_o are measured in W/m^2, LAI units are in m^2/m^2, f_{PAR} is dimensionless (0 to 1), and k_p is the light extinction coefficient (dimensionless). The f_{PAR} variable indicates the ratio of the incoming PAR flux that is attenuated within the canopy and that reaches the ground surface. Thus, f_c is often defined as "$1 - f_{PAR}$", the fraction of PAR flux absorbed or intercepted by the plant elements, as indicated in [26].

The k_p parameter has its physical meaning associated with the decay rate of the PAR irradiance within the canopy [27] and serves as an input for forest and canopy growth modeling [28,29], evapotranspiration estimation using surface energy balance approaches [30–33], ecosystem flux modeling [34], and spectral pixel decomposition into soil and vegetation composites [35]. Furthermore, the parameter k_p depends on the canopy structure elements, the position of the sun relative to the ground surface at a given time of the day, and the multispectral light leaf response [36–39]. Typical values of k_p for crops range from 0.30 to 1.50 and are associated with a given canopy species type [40]. For maize [41] (*Zea Mays* L.), reported k_p values in the literature vary from 0.40 to 0.72 when maize is fully developed at maximum LAI values [42–44].

Direct measurements of k_p are not feasible due to a lack of specific instrumentation to obtain on-site data. Thus, on-site k_p values are often retrieved by solving Equations (1) and (2) for k_p with measurements of φ_o, φ_{down}, and the LAI as inputs [45]. Measurements of f_{PAR} are commonly performed using PAR detectors above the canopy and at the ground surface level. LAI measurements are commonly performed using destructive [46–48] and non-destructive [9,46,49,50] techniques. Even though LAI and f_{PAR} measurements are widely used in environmental studies, they are often tedious, and the data collection is labor intensive [51]. When it comes to agricultural fields in particular, surface heterogeneity conditions (e.g., soil water status, soil texture, soil salinity, soil compaction, differences in canopy architecture development, cropland field layout) are often present, and they require extensive sampling locations (point-based data) to accurately represent the inherent spatial variability in cropland fields [52,53]. Thus, modeling k_p has been used to obtain estimates of the characteristics of light attenuation in vegetated surfaces for the past 44 years [27,33,36,45,54–59].

In Japan, ref. [58] developed a k_p model for maize and rice using a locally calibrated linear model that had the LAI as a predictor. Ref. [27] developed a model for k_p that assumes an ellipsoidal inclination angle distribution for plant canopies and uses the leaf geometry ratio between horizontal and vertical projections and the solar zenith angle as predictors. The overall accuracy of [27] k_p model, in terms of the root mean square error (RMSE), was between 0.004 and 0.01 for data obtained in maize, soybeans, and sunflower canopies in England. Ref. [36] developed semi-empirical models for f_{PAR} using different vegetation indices and provided linear models that relate k_p to an equivalent light extinction coefficient derived for a given vegetation index using local data from sugar beet and wheat fields in France and Netherlands. Ref. [55] linearly modeled k_p using the normalized-difference vegetation index (NDVI) as a predictor for watershed plant growth modeling. Ref. [55] modeled plant growth using the Soil and Water Assessment Tool (SWAT) and found that k_p had a large spatial variability at a regional scale, with k_p values ranging from 0.03 to 2.90 across a wide range of vegetation cover types (e.g., coniferous trees, broad-leaved forests, shrubs, and others).

Ref. [56] estimated k_p for apple orchards in Chile through an exponential model using f_c as a predictor and found that the non-linear k_p model improved the estimation of the LAI by 28% compared to a tabulated or constant value of k_p for apple trees. Ref. [59] used the k_p model from [36] to estimate k_p for a wide range of urban heterogeneous forest types in Washington, USA, using light detection and ranging (LIDAR) aerial data and found that the "canopy gap fraction" approach based on Beer's law [24], which assumes localized surface homogeneity, does not accurately represent urban scenarios where tree heterogeneity is significant. Ref. [45] used machine-learning regression as a random forest algorithm to predict the LAI and k_p for deciduous forests in India using Landsat-8 multispectral data. They found that the machine-learning algorithm predictions of k_p had a normalized RMSE or NRMSE of 12% and explained 77% of the variability in observed k_p. Ref. [57] investigated the use of a combined "canopy gap fraction" and NDVI to estimate the LAI for three wheat crop varieties with different leaf angle orientations (e.g., erectophile, planophile, and middle types). They found that k_p and NDVI were inversely and linearly related to the fitted k_p model, explaining 88% to 91% of the variability in observed wheat k_p across the three crop varieties. Ref. [54] estimated f_{PAR} for maize fields in Argentina using seven crop genotypes and five different k_p modeling approaches based on non-linear regression and Bayesian models. They found that the five k_p models developed did not perform well when estimating f_{PAR} since f_{PAR} values were outside the 0 to 1 range of expected values, and k_p estimation was unrealistic for typical maize values published in the literature. Ref. [54] indicated that statistical models like Bayesian modeling approaches must be used cautiously when predicting f_{PAR} and k_p.

Even though several studies provide different modeling approaches to k_p for specific vegetation types, significant issues impede the use of these models in cropland fields. First, most k_p published models are purely empirical and have the limitation of being suitable for conditions that resemble the initial data used to calibrate the model. Second, the spatial heterogeneity of agricultural fields often presents challenges in accurately determining canopy structure and k_p. The complexity of k_p being influenced by different irrigation water management practices and crop row layouts has been the center of discussion in previous publications concerning maize, sorghum, soybean, and sunflower canopies [43,60]. A study [60] indicated that under varying conditions of soil moisture (a surrogate for changing canopy structure), the k_p variable depends on the differences in the spatiotemporal canopy structure (e.g., the LAI or f_c) and might be subject to variability within cropland fields. Ref. [43] showed a linear decrease in k_p as the crop row layout increased.

To our current knowledge, there has never been a study that attempted to develop a semi-empirical spatial model for maize k_p that incorporates multiple canopy architecture features (e.g., the LAI and f_c) and NDVI composites for soil and vegetation using data from several different multispectral remote sensing platforms. The inherent non-linear nature of light transmission, absorption, and scattering within a surface requires more sophisticated approaches to describe the canopy structure in agricultural fields. For row crops such as maize, partial canopy cover conditions are predominant throughout the growing season, and partitioning the ground surface between soil and plants is critical to enhance environmental physics modeling [61]. Maize is one of the major commodities in the United States (USA) and around the globe, supporting the food production, energy, and forage sectors of the local and global economy [62]. With the advent of climate change through global warming scenarios [63] indicated that a 29% loss in maize yield in the USA would be related to extreme drought events in the next thirty-five years. Thus, finding ways to advance spatial modeling of maize environmental properties, such as k_p, is critical to improving cropland management practices focusing on the sustainable use of water and nutrients, pest infestation detection, and crop yield optimization.

Hence, this study aimed to: (a) develop a novel semi-empirical model for maize k_p estimation using multiple canopy architecture features (i.e., LAI and f_c) and NDVI partitioning into soil and canopy composites derived from multispectral data from several remote sensing (RS) platforms (e.g., spaceborne, airborne, and proximal); (b) independently evaluate the performance of the proposed semi-empirical maize k_p model, comparing it to the most used k_p approach from [27]; and (c) run a sensitivity analysis to identify the most critical variables that add uncertainty to the semi-empirical maize k_p predictions.

2. Materials and Methods

2.1. The Novel Maize Light Extinction Coefficient Model

When rearranging Equation (1), k_p might be calculated as indicated by Equation (3) [22]:

$$k_p = -\left(\frac{1}{\text{LAI}}\right) \times \ln(f_{\text{PAR}}) \tag{3}$$

In Equation (3), k_p depends on the LAI and f_{PAR} as inputs. While LAI estimates can be obtained for maize using previously published or locally calibrated models (e.g., [64,65]), f_{PAR} estimation is often performed by taking k_p as one input [36,38]. Thus, Equation (3) is often used to derive "measured" k_p values obtained using the measured (or estimated) LAI and measured f_{PAR} as inputs. Thus, k_p needs to be modeled apart from f_{PAR}. Assuming that k_p could be linearly associated with an equivalent light extinction coefficient (k_v) from vegetation indices [36], the k_p modeling is given by Equation (4):

$$k_p = \beta_1 \times k_v + \beta_o \tag{4}$$

where k_v is dimensionless; the β_o and β_1 parameters are the fitted intercept and slope of the linear model for k_p. Ref. [36] showed that k_p and k_v could be scaled by a constant when deriving semi-empirical calibrated functions for determining the fractional light transmittance from partitioned vegetation indices into soil and vegetation components.

The k_v variable is determined from a non-linear vegetation index decomposition model based on the modified Beer–Lambert law and indicated by Equation (5) [66–70]:

$$\text{VI} = \text{VI}_c + (\text{VI}_{\text{soil}} - \text{VI}_c) \times \exp(-k_v \times \text{LAI}) \tag{5}$$

where VI refers to a given vegetation index and VI_c, and VI_{soil} are the VI values for bare soil (f_c = 0) and fully vegetated (f_c = 1) canopies.

For most environmental applications in the "canopy gap fraction" theory, NDVI has shown to be a strong predictor (e.g., [68,71]). Thus, this study considered NDVI to calculate k_v as the VI variable in Equation (5). When rearranging Equation (5), k_v is calculated as indicated by Equation (6) [69]:

$$k_v = -\left(\frac{1}{\text{LAI}}\right) \times \ln\left(\frac{\text{NDVI} - \text{NDVI}_c}{\text{NDVI}_{\text{soil}} - \text{NDVI}_c}\right) \tag{6}$$

where $NDVI_{soil}$ and $NDVI_c$ are the NDVI values for bare soil and fully vegetated conditions, respectively.

The main issue with Equation (6) is determining $NDVI_{soil}$ and $NDVI_c$ spatial estimates. Ref. [72] indicated that most of the studies that require $NDVI_{soil}$ and $NDVI_c$ as input data use fixed values based on statistical thresholds from histogram analysis (e.g., [36,73–75]). However, spatial variability in soil and canopy features is often present in cropland fields, which does not support the assumption of a constant value of $NDVI_{soil}$ and $NDVI_c$ for most real field conditions. Furthermore, ref. [66] indicate that $NDVI_{soil}$ is a function of the shallow soil layer's soil texture, roughness, and water content conditions. Hence, this study proposes to determine $NDVI_{soil}$ and $NDVI_c$ indirectly using NDVI data for a given day of multispectral remote sensing (RS) imagery (space- or air-borne) or proximal (near surface) discrete data acquisition.

The $NDVI_{soil}$ and $NDVI_c$ are related to f_c through a unique semi-empirical and quadratic function of NDVI, as indicated by Equation (7) [10,68,71]:

$$f_c = \left(\frac{NDVI - NDVI_{soil}}{NDVI_c - NDVI_{soil}} \right)^2 \tag{7}$$

Rearranging Equation (7) provides an expression for NDVI as a function of f_c, $NDVI_{soil}$, and $NDVI_c$, as indicated by Equation (8) below:

$$NDVI = \sqrt{f_c} \times NDVI_c + \left(1 - \sqrt{f_c}\right) \times NDVI_{soil} \tag{8}$$

In Equation (8), the only unknown variables are $NDVI_{soil}$ and $NDVI_c$ since NDVI and f_c are calculated from the multispectral data of a given remote sensing platform. Thus, when differentiating Equation (8) concerning f_c, the following equation for the $NDVI_c$ and $NDVI_{soil}$ difference is given as indicated by Equation (9):

$$NDVI_c - NDVI_{soil} = 2 \times \sqrt{f_c} \times \frac{d}{df_c}(NDVI) \tag{9}$$

where $\frac{d}{df_c}(NDVI)$ is the first-order derivative of NDVI with respect to f_c. Substituting Equation (9) into Equation (8) gives the following models for calculating $NDVI_{soil}$ and $NDVI_c$, as indicated by Equations (10) and (11), respectively:

$$NDVI_{soil} = NDVI - 2 \times f_c \times \frac{d}{df_c}(NDVI) \tag{10}$$

$$NDVI_c = NDVI + 2 \times \left(\sqrt{f_c} - f_c\right) \times \frac{d}{df_c}(NDVI) \tag{11}$$

In Equations (10) and (11), the only unknown variable is $\frac{d}{df_c}(NDVI)$. Thus, it is imperative to determine a way to calculate this first-order derivative of NDVI regarding f_c. In this study, we followed a procedure similar to that proposed by [76] to obtain $\frac{d}{df_c}(NDVI)$ for each imagery pixel or for point-based proximal RS data from a given RS platform. The following steps were taken to derive an empirical model for $\frac{d}{df_c}(NDVI)$:

- Using a multispectral image or point-based data within agricultural fields and for a given remote sensing platform, the measured f_c is divided into f_c intervals. Minimum ($NDVI_{min}$) and maximum ($NDVI_{max}$) values of NDVI are recorded for each f_c interval, as well as their respective f_c values. Each f_c interval provides two pairs of points ($NDVI_{min}$, $f_{c,min}$) and ($NDVI_{max}$, $f_{c,max}$).
- Across all measured f_c data intervals, the pair of points ($NDVI_{min}$, $f_{c,min}$) are linearly regressed to obtain $\frac{d}{df_c}(NDVI_{min})$, which is given as the slope of the linear function $NDVI_{min} = g(f_{c,min})$. Similarly, a process is followed to derive $\frac{d}{df_c}(NDVI_{max})$ using the ($NDVI_{max}$, $f_{c,max}$) points across the f_c data intervals.
- With values of $\frac{d}{df_c}(NDVI_{min})$ and $\frac{d}{df_c}(NDVI_{max})$ at $f_{c,min}$ and $f_{c,max}$ observed values, respectively, $\frac{d}{df_c}(NDVI)$ is linearly interpolated for every pixel or for point-based multispectral data for the remaining values of f_c within the range [$f_{c,min}$, $f_{c,max}$].

Hence, the linear interpolation model for $\frac{d}{df_c}$(NDVI) is given by Equation (12) below:

$$\begin{aligned}\frac{d}{df_c}(\mathrm{NDVI}) = &\frac{d}{df_c}(\mathrm{NDVI_{min}}) \\ &-\left(\frac{f_{c,min}-f_c}{f_{c,min}-f_{c,max}}\right)\times\left[\frac{d}{df_c}(\mathrm{NDVI_{min}})-\frac{d}{df_c}(\mathrm{NDVI_{max}})\right]\end{aligned} \quad (12)$$

The summary of the steps of the procedure followed to obtain the novel semi-empirical approach for maize k_p are provided in Figure 1. Essentially, the primary inputs for spatially predicting k_p are the LAI, f_c, $\mathrm{NDVI_{soil}}$, and $\mathrm{NDVI_c}$ (both NDVI composites as a function of f_c).

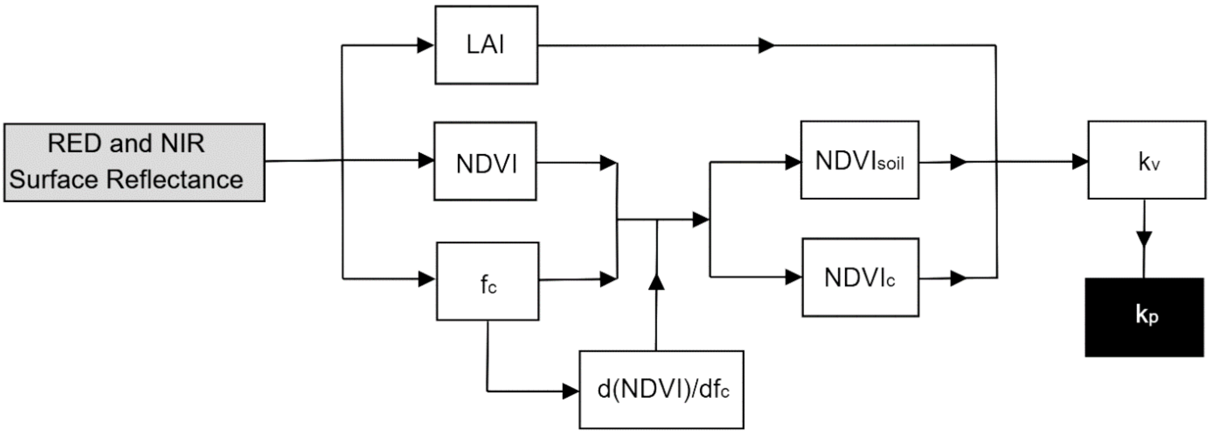

Figure 1. Flowchart of the novel spatial k_p modeling approach.

2.2. The General Light Extinction Model

The [27] general light extinction model was initially developed using an ellipsoidal inclination angle distribution for plant leaves based on the following assumptions: k_p represents the ratio between the projected horizontal shadow cast and the leaf area [77]. The leaf area distribution of most vegetated canopies can have a spherical, cylindrical, or conical shape [78]. By assuming a spherical leaf area distribution with a vertical and horizontal axis, ref. [27] derived the general k_p model for any vegetated canopy, as shown in Equation (13) below:

$$k_p^{[C]} = \begin{cases} \dfrac{\sqrt{\xi^2+\frac{1}{\tan^2(90^\circ-\Omega)}}}{\xi+\frac{\sin^{-1}(\epsilon_2)}{\epsilon_2}}, & \xi < 1 \\ \dfrac{\sqrt{\xi^2+\frac{1}{\tan^2(90^\circ-\Omega)}}}{\xi+0.50\times\epsilon_1\times\xi\times\ln\left(\frac{1+\epsilon_1}{1-\epsilon_1}\right)}, & \xi \geq 1 \end{cases} \quad (13)$$

where the superscript [C] refers to the k_p model presented in [27]; Ω is the solar zenith angle (radians); ξ is the leaf distribution parameter (i.e., the ratio between the projected area of a leaf on the horizontal and vertical planes); and ϵ_1 and ϵ_2 are auxiliary parameters that are calculated as indicated by Equations (14) and (15), respectively [27,79]:

$$\epsilon_1 = \sqrt{1-\xi^2} \quad (14)$$

$$\epsilon_2 = \sqrt{1-\xi^{-2}} \quad (15)$$

Ideally, the ξ ratio is calculated using measured horizontal and vertical leaf lengths. However, such measurements on a spatial basis are impractical. Thus, it is often assumed that the ξ is nearly constant for homogeneous vegetated surfaces [27]. For maize, it was assumed that ξ = 1.64 as the mean tabular value from [80].

Ref. [27] indicated that when $\xi = 1$ (circular shape), Equation (13) is simplified and indicated by Equation (17):

$$k_p^{[SC]} = \frac{1}{2 \times \sin(90^\circ - \Omega)} \tag{16}$$

where the superscript [SC] refers to the simplified k_p model in [27].

2.3. Calculation of Vegetation Indices

The NDVI, LAI from [65], and OSAVI vegetation indices were calculated by Equations (17)–(19), respectively:

$$\mathrm{NDVI} = \frac{\mathrm{NIR} - \mathrm{RED}}{\mathrm{NIR} + \mathrm{RED}} \tag{17}$$

$$\mathrm{LAI} = 0.263 \times \exp(3.813 \times \mathrm{OSAVI}) \tag{18}$$

$$\mathrm{OSAVI} = \frac{\mathrm{NIR} - \mathrm{RED}}{\mathrm{NIR} + \mathrm{RED} + 0.16} \times 1.16 \tag{19}$$

where NIR and RED are the surface reflectance data in the near infrared and red bandwidths of the electro-magnetic spectrum of a given RS platform (dimensionless) and OSAVI is the optimized soil adjusted vegetation index. LAI is measured in m^2/m^2.

The f_c model used in this study is the non-linear approach developed by [31,32], in which f_c is calculated as an exponential function of the LAI adjusted for canopy clumped conditions (such as maize) where canopy leaves are randomly distributed above the ground surface. The models associated with predicting f_c are presented by Equations (20)–(24) [31,32]:

$$f_{c,o} = 1 - \exp(-0.50\ \mathrm{LAI}) \tag{20}$$

$$\mathrm{LAI_L} = \mathrm{LAI}/f_{c,o} \tag{21}$$

$$f_s = 1 + f_{c,o} \times \exp(-0.50\ \mathrm{LAI_L}) - f_{c,o} \tag{22}$$

$$\mathrm{CF} = -\ln\left(\frac{f_s}{0.50\ \mathrm{LAI}}\right) \tag{23}$$

$$f_c = 1 - \exp(-0.50 \times \mathrm{CF} \times \mathrm{LAI}) \tag{24}$$

where $f_{c,o}$ is the initial f_c value before adjustments (dimensionless); $\mathrm{LAI_L}$ is the local LAI (m^2/m^2); f_s is the soil fractional cover (dimensionless); and CF is the vegetation clumping factor (dimensionless).

2.4. Research Sites

2.4.1. Limited Irrigation Research Farm (LIRF)

The Limited Irrigation Research Farm (LIRF) is located near Greeley, Colorado, USA, at 40.4463°N, longitude 104.6371°W, and 1432 m above sea level (ASL). The LIRF is managed by the United States Department of Agriculture (USDA)—Agricultural Research Service (ARS). The LIRF site has a subtropical steppe with a cold semiarid area [81]. Two adjacent rectangular maize fields (190 m × 110 m) were used for data collection during the months of July to September in 2018, 2020, and 2022 (Figure 2). The field had irrigation events scheduled every time the soil water depletion, in the crop root zone, approached the selected volumetric soil water content for management-allowed depletion (MAD) for maize. This MAD value was 60% of the total available water (TAW) at the LIRF location.

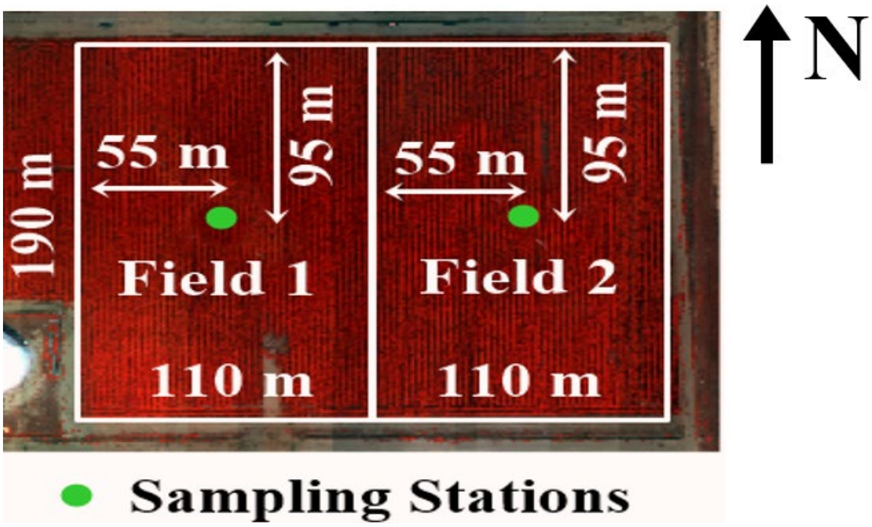

Figure 2. The LIRF experiment site in 2017, 2018, 2020, and 2021. The sampling locations provided concurrent measurements of the LAI, f_{PAR}, and h_c. In 2020 (Field 1) and 2021 (Field 2), only one sampling location at the frequently irrigated field was part of the experiment design. In 2017 and 2018, each field had its sampling station for maize canopy architecture data. The red areas are vegetation.

Both maize fields at LIRF had subsurface drip irrigation with buried drip laterals 0.23 m deep and emitters spaced every 0.30 m. The maize row orientation was north–south, with rows 76 cm apart and two consecutive maize plants 17 cm apart. The maize planting density was 87,500 plants/ha during all years of data collection. In 2017 and 2018, the maize variety was Dekalb 51–20 in each field. In 2020, NK9227-5222A (Syngenta Inc., Basel, Switzerland) was the maize variety, while in 2021, three maize varieties, P9998Q, and P0157AMXT (Pioneer Hi-Bred International, Inc., Johnston, IA, USA), and CH 194-49 DG (Channel Bio Corporation, Saint Louis, MO, USA), were seeded across each field, with approximately 83% of each treatment plot covered by the maize variety P0157AMXT (Figure 3). Regardless of the maize type, all varieties were drought-tolerant.

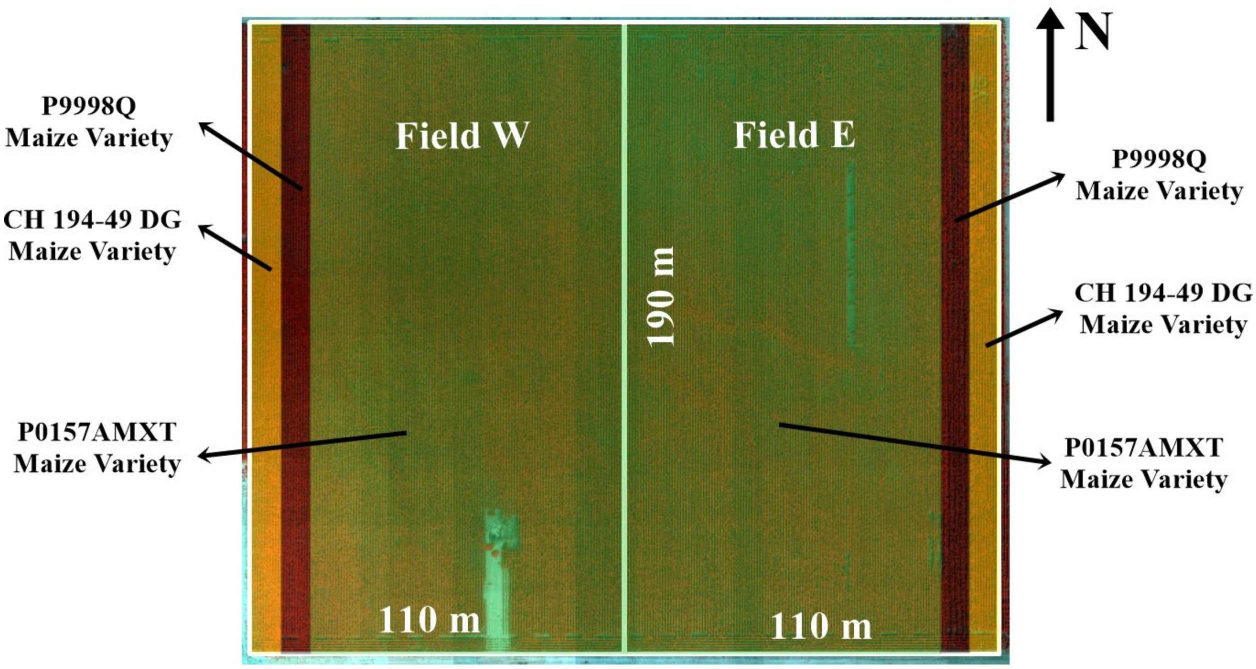

Figure 3. Maize varieties at the LIRF in 2021.

Irrigation scheduling was based on the United Nations paper FAO-56 Irrigation and Drainage: Crop Evapotranspiration [82], which uses a dual crop coefficient and reference alfalfa evapotranspiration (ET_r). The ET_r data were calculated as indicated by [83] as well. The basal maize crop coefficient (K_{cb}) was determined as a local K_{cb} following the approach of [84]. The stress coefficient (k_s) for the low-frequency irrigation field was calculated using the relationship between the total available water (TAW), readily available water (RAW), and soil water deficit (D_r) from [83].

2.4.2. Irrigation Innovation Consortium (IIC)

The IIC site was in Fort Collins, Colorado, USA, at 40.5542°N latitude, 105.0038°W longitude, and 1486 m ASL. The IIC site has a local climate classified as subtropical steppe and cold semiarid [81]. Data collection happened on a surface-irrigated maize field (furrow) from July to September in 2020 and 2021 (Figure 4). The maize field has a surface area of 64,750 m^2, with an east–west maize row orientation and 76 cm row spacing. The field has a uniform sandy loam soil texture with VWC_{FC}, VWC_{PWP}, and VWC_{SAT} equal to 0.189, 0.069, and 0.410 m^3/m^3, respectively. Several 4 cm-diameter aluminum siphon tubes provided water from the irrigation ditch to the furrows in the field. The irrigation waterfront moved from the east (central channel) to the west.

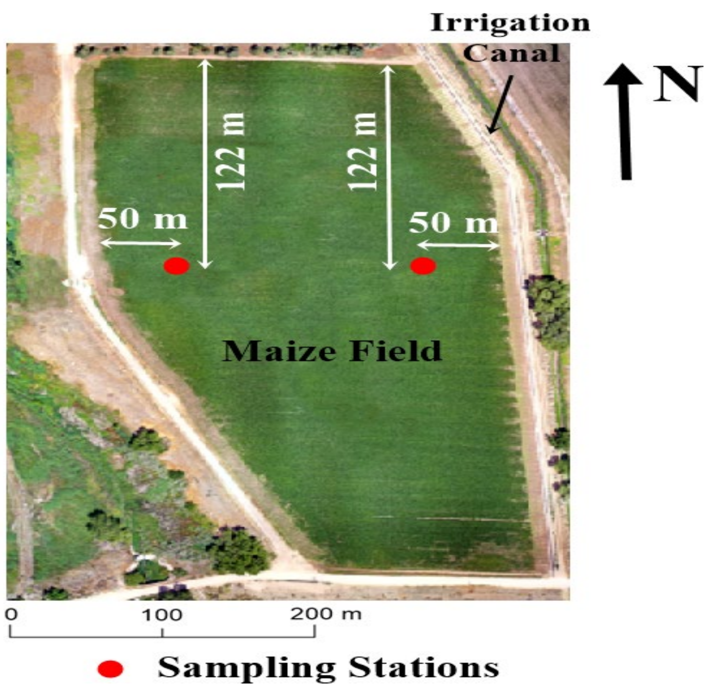

Figure 4. The IIC experiment site in 2020 and 2021. The sampling locations provided concurrent measurements of the LAI and h_c. The f_{PAR} measurement station is located on the field's east side. The green areas are vegetation.

Different maize varieties were planted in 2020 and 2021. The G02K39-3120 (Golden Harvest, Minnetonka, MN, USA) variety was planted on 13 May 2020 at an 8 seeds/m^2 seeding rate. In 2021, the maize varieties NK0243-3120 and NK0314-5122 (Syngenta AG, Basel, Switzerland) were planted at the same seeding rate as in 2020. The seeding date was 13 May 2021. All maize varieties in this study were classified as drought tolerant. The irrigation application efficiency of the surface furrow system was assumed to be 50% during each year of data collection based on common local practices. The irrigation events occurred two to three days after water acquisition from the Sand Dike Lateral (Canal) Company (Fort Collins, CO, USA) and lasted 6 to 12 h.

2.5. On-Site Data Collection

2.5.1. Multispectral Surface Reflectance Data

Landsat-8 Operational Land Imager Level-2

Landsat-8 is managed by the United States Geological Service (USGS) and the National Space Agency (NASA) and has an operational land imager (OLI) and a thermal infrared sensor (TIRS) that provide biweekly multispectral data at 30 m and 100 m spatial resolutions, respectively. The OLI sensor provides short-wave multispectral data in the visible (red, green, and blue bands) and invisible light spectrum (for instance, short-wave infrared (SWIR) or near infrared (NIR)). Since the LIRF and IIC maize fields are located within the overlap region of Landsat-8 path/row 33/32 and 34/32 scenes, the revisiting time for the research sites was 8 days. In this study, surface reflectance data acquired with the red (655 ± 30 nm) and NIR (870 ± 30 nm) Landsat-8 bands, acquired during clear-sky days, were used to derive the vegetation indices.

The Landsat-8 satellite has a sun-synchronous orbit around Earth (705 km altitude) and overpasses our research sites at approximately 11:30 am MST local time. The final radiometric resolution of Landsat-8 imagery is 16 bits. The metadata imagery file provides linear calibration coefficients to convert a digital number (DN) to surface reflectance and nadir-looking surface temperature (T_s) for Landsat-8 Level 2 imagery. The Level 2 images undergo rigorous calibration procedures and do not require further post-processing after the final surface reflectance and temperature images are appropriately converted from the original DN values [85]. The conversion from DN to surface reflectance for Landsat-8 Level 2 products is given by Equation (25) below [86]:

$$\mathrm{SR_i^{[L8]}} = 0.0000275 \times \mathrm{DN_i} - 0.20 \quad (25)$$

where $\mathrm{SR_i^{[L8]}}$ is the surface reflectance of a given ith multispectral band in the visible and invisible light spectrum (dimensionless, from 0 to 1) and $\mathrm{DN_i}$ is the DN of the respective ith band (dimensionless). The superscript L8 alludes to the Landsat-8 remote sensing platform.

Sentinel-2 Level 2

Sentinel-2 is a spaceborne RS platform managed by the European Space Agency (ESA). The Sentinel-2 satellites S2A and S2B provide optical multispectral imagery of Earth's landscape every ten days from satellites orbiting around the equator. The revisiting time is reduced by half when the two sets of satellite data are used for applications. If a given area of interest is located at middle latitudes, the Sentinel-2 temporal resolution is two to three days, considering data from S2A and S2B for specific regions that have aerial overlap.

The S2A and S2B satellites also have a sun-synchronous orbit (786 km altitude), and they take images of Earth near noon (local time) for our research sites. Sentinel-2 images have varying spatial resolutions depending on the optical multispectral bands. This study used cloud-free images, and only the red (665 ± 31 nm) and NIR (833 ± 106 nm) Sentinel-2 bands, with an imagery pixel size (spatial resolution) of 10 m, were utilized. The final radiometric resolution of Sentinel-2 images is 16 bits. The pre-processing stages of the Sentinel-2 data include atmospheric corrections using a radiative transfer approach performed by the ESA named Sen2Cor [87,88]. The surface reflectance data were scaled by a factor of 10,000 as the final output. Thus, the calculation of surface reflectance as a fraction (0 to 1) for each optical multispectral band is obtained as indicated in Equation (26) below:

$$\mathrm{SR_i^{[S2]}} = 0.0001 \times \mathrm{SR_{i,sc}^{[S2]}} \quad (26)$$

where $\mathrm{SR_i^{[S2]}}$ is the fractional surface reflectance from Sentinel-2 for an ith band (dimensionless, from 0 to 1) and $\mathrm{SR_{i,sc}^{[S2]}}$ is the scaled surface reflectance data for an ith band provided by ESA imagery (dimensionless). The [S2] superscript alludes to the Sentinel-2 remote sensing platform.

Planet CubeSat

Planet CubeSat is a privately-owned constellation of mini satellites developed and operated by Planet Labs (Planet Labs, Inc., San Francisco, CA, USA). There are more than 130 CubeSat units surveying Earth's landscape every day, with 3 m (nominal) spatial resolution imagery products [89]. Similarly to Landsat-8 and Sentinel-2, the final radiometric resolution of Planet CubeSat is 16-bit. Planet CubeSat satellites are considered low-cost due to their compact design (0.10 m $\times$ 0.10 m $\times$ 0.30 m and 4 kg weight). The CubeSat satellites are sun-synchronous (altitude ranging from 450 km to 580 km) and have an overpass time varying from 9:30 to 11:30 a.m. local time [89] for our research sites.

The Planet CubeSat imagery data undergoes atmospheric corrections to minimize the effects of atmospheric gases and aerosols on the quality of the imagery (e.g., light scattering). To correct CubeSat imagery data for aerosol and gas disturbance of the surface-originated (reflected) light, the Moderate Resolution Imaging Spectroradiometer (MODIS) water vapor, ozone, and aerosol quality control products are used to improve the calibration of Planet CubeSat imagery using the 6SV2.1 radiative transfer model; this is because Planet CubeSat satellites do not have these products [89]. However, the atmospheric corrections performed by Planet Labs do not include correction for the effects of stray light, haze, and thin cirrus clouds. It also assumes that Earth's landscape is a quasi-Lambertian surface (e.g., where light is scattered homogeneously in all possible three-dimensional directions) and that all imagery scenes have the same sea-level altitude [89].

This study used the CubeSat imagery scenes as the Sentinel-2 harmonized surface reflectance products released by Planet Labs. The harmonization process is based on the work of [90,91], in which Planet CubeSat imagery data was cross-validated using Sentinel-2 data to minimize signaling differences among different CubeSat satellite units (e.g., Dove-R, SuperDove, Dove Classic) and to improve surface reflectance data to a standard similar to Sentinel-2 multispectral data. In this study, only the harmonized red (666 $\pm$ 80 nm) and NIR (867 $\pm$ 80 nm) bands from Planet CubeSat were used as input data when imagery was acquired only during clear-sky days.

The calculation of surface reflectance as a fraction (0 to 1) for each optical Planet CubeSat multispectral band is performed using Equation (27) below:

$$\mathrm{SR}_{\mathrm{i}}^{[\mathrm{CS}]} = 0.0001 \times \mathrm{SR}_{\mathrm{i,sc}}^{[\mathrm{CS}]} \quad (27)$$

where $\mathrm{SR}_{\mathrm{i}}^{[\mathrm{CS}]}$ is the fractional surface reflectance from the Planet CubeSat for an ith band (dimensionless, from 0 to 1) and $\mathrm{SR}_{\mathrm{i,sc}}^{[\mathrm{CS}]}$ is the scaled surface reflectance data for an ith band provided (dimensionless). The [CS] superscript alludes to the Planet CubeSat RS platform.

Multispectral Handheld Radiometer

A handheld multispectral radiometer (MSR5, CropScan Inc., Rochester, MN, USA) provided ground-based surface reflectance measurements. An MSR5 multispectral radiometer consists of a radiometer unit mounted on a telescopic pole that measures nadir-looking incoming and outgoing radiation within the visible and invisible light spectrum above the canopy surface. The MSR5 radiometer has a field-of-view (FOV) of 28°. The MSR5 data measurements were collected at each sampling location and at each research site with the MSR5 sensor positioned at 2.2 m AGS. The MSR5 equivalent ground sampling area (footprint) represented a 1 m-diameter circumference for a 2V:1H (vertical to horizontal relative ratio) instrument footprint. The MSR5 is a passive sensor that provides "point" or "discrete" data and has the same band characteristics as Landsat-5 multispectral bands in the visible and invisible light spectrum for the surface reflectance data only. MSR5 multispectral data were acquired weekly (IIC 2020, LIRF 2020, and 2021) and biweekly (LIRF 2018 and IIC 2021) from July to September. Four readings were taken with the MSR5 at the row and inter-row (and later averaged) at each sampling location. In this study, only MSR5 red (560 $\pm$ 60 nm) and NIR (830 $\pm$ 140 nm) bands were used as input data.

Unmanned Aerial System

Unmanned aerial systems (UAS) were also used in this study. UAS-based data acquisition missions (flights) were systematically arranged for the two research sites. The flight plans were developed and executed by the USDA-ARS Water Management and Systems Research Unit and the Colorado State University (CSU) Drone Center. The USDA-ARS division managed the acquisition and data processing of UAS imagery for the LIRF site, while the CSU Drone Center was responsible for the IIC site UAS data collection and pre-processing. The aerial imagery data were collected using a MicaSense RedEdge-MX multispectral camera (MicaSense Inc., Seattle, WA, USA). The RedEdge-MX sensor encompasses four spectral bands: blue (475 nm, 32 nm bandwidth), green (560 nm, 27 nm bandwidth), red (668 nm, 14 nm bandwidth), and NIR (842 nm, 57 nm bandwidth). The UAS red and NIR datasets were used in this study to calculate the spectral vegetation indices. UAS imagery was post-processed using ArcGIS 10.8 (ESRI, Redlands, CA, USA).

The IIC UAS multispectral data had a pixel spatial resolution of 0.08 m and underwent processing using Pix4D v4.5.6 software (Pix4D S.A., Prilly, Switzerland). The imagery individual frame overlap and sidelap percentages were 80 and 70, respectively. At the LIRF site, the finalized multispectral outputs attained a pixel spatial resolution of 0.03 m, with overlap and sidelap percentages of 88 and 70, respectively. The LIRF imagery was processed using Agisoft Metashape software (Agisoft Metashape Pro version 1.6.4 software, Agisoft LLC, St. Petersburg, Russia). The UAS-derived surface reflectance data were combined with nadir-looking T_s data from SI-111 stationary sensors (Apogee Instruments Inc., Logan, UT, USA) obtained from point-based measurements at each research site, serving as RS input data for this investigation.

Measured Leaf Area Index (LAI)

Maize LAI measurements were acquired on a weekly basis using the LAI-2200C Plant Canopy Analyzer (LI-COR Biosciences, Lincoln, NE, USA), a modern and non-destructive instrument designed for point-based measurements of canopy foliage architecture. The LAI measurements were obtained at each LIRF and IIC maize field sampling location. Six readings per station were taken, moving the sensor about 20 cm in a diagonal transect between the crop rows starting closer to one row and ending closing to the next row; then, during data post-processing, those six readings were averaged to produce a single LAI value per station. The LAI-2200 analyzer utilized a unique combination of upward and downward sensors, with passive and optical parts and five concentric detectors measuring diffuse light transmittance above and within the canopy at five different zenith angles.

A cubic convolution gap-filling approach was utilized to provide temporal interpolated LAI data for the days without measurements during the period studied, similar to the interpolation methods implemented by [92,93]. The interpolation method for the measured LAI was explicitly applied to each data collection time series per measurement station within the frequently irrigated fields at the LIRF and IIC. Temporal extrapolation of vegetation indices assumes that for irrigated fields with no lack of nutrients, water availability, and pristine vegetation, the changes in canopy leaf arrangements are minimal within shorter periods under similar environmental conditions (e.g., cloudless skies, stable air temperature and wind speed, etc.).

2.5.2. Measured Fractional Canopy Cover (f_c)

At the LIRF and IIC, indirect measurements of f_c aimed at assessing the vegetation conditions were used to determine the observed k_p values and evaluate the errors associated with predicting f_c. An LI-190R PAR sensor and LI-191R line quantum LPAR sensor (LI-COR Biosciences, Lincoln, NE, USA) connected with a CR3000 datalogger (Campbell Scientific Inc., Logan, UT, USA) measured the above- and below-canopy photosynthetically active radiation (PAR), respectively. The instruments were placed in the frequently irrigated fields at the LIRF (Field W in 2020 and Field E in 2021) and IIC (Field F). The PAR data were recorded at 1 min and averaged every 15 min. The LI-190R sensor was mounted on a 4 m-tall vertical post 3.5 m above the ground surface (AGS). The LI-190R and LI-191R line quantum sensors are widely utilized instruments for precise measurements of green vegetation cover. The LI-190R is an upward-facing sensor that measures incident PAR light, while the LI-191R is a sensor designed to measure transmitted PAR light through the vegetation canopy. Both sensors operate within the 400–700 nm PAR wavelength range. Indirect "measurements" of f_c are obtained through the application of Equation (28) as follows:

$$f_c = 1 - \frac{PAR_{below}}{PAR_{above}} \tag{28}$$

where PAR_{below} means the PAR radiation measured at the ground surface level with the LI-191R line quantum sensor (μmol/s/m^2) and PAR_{above} means the PAR radiation measured above the canopy (μmol/s/m^2).

2.6. Statistical Analysis

2.6.1. Error Metrics

The following statistical variables were used to evaluate the performance of the models in this study: mean bias error (MBE), root mean square error (RMSE), normalized MBE (NMBE), normalized RMSE (NRMSE), and the coefficient of determination (R^2). Equations (29)–(32) indicate MBE, NMBE, RMSE, and NRMSE, respectively:

$$MBE = \left(\frac{1}{n}\right)\sum_{i=1}^{n}(E_i - O_i) \tag{29}$$

$$NMBE = \left(\frac{MBE}{\overline{O}}\right) \times 100\% \tag{30}$$

$$RMSE = \sqrt{\left(\frac{1}{n}\right)\sum_{i=1}^{n}(E_i - O_i)^2} \tag{31}$$

$$NRMSE = \left(\frac{RMSE}{\overline{O}}\right) \times 100\% \tag{32}$$

where $\overline{O}$ is the mean of the observed data, n is the sample size, and E_i and O_i are the estimated and observed values, respectively. NMBE and NRMSE are given in percentages, while Equations (29) and (31) provide statistical indicators with the same units as the primary variables.

The R^2, in the context of model performance assessment, informs about the degree of variability in the observed data explained by the modeling approach. Equation (33) gives the mathematical expression for R^2:

$$R^2 = \frac{\sum(E_i - \overline{E})(O_i - \overline{O})}{\sqrt{\left[\sum(E_i - \overline{E})^2\right]\left[\sum(O_i - \overline{O})^2\right]}} \tag{33}$$

where $\overline{E}$ is the mean value of the predictions.

2.6.2. Global Sensitivity Analysis

The Sobol global sensitivity (SGS) approach [94,95] is based on quantifying uncertainty to determine the impact of any given input parameters in a mathematical model over the entire input parameter space. The SGS technique uses variance-based metrics to assess the contribution of individual parameters to the total variance in the model prediction output. By decomposing the total variance in the model output into components attributed to individual parameters and their combinations, the Sobol indices offer a quantitative measure of global sensitivity for a given model. These Sobol indices provide insights into which parameters are more relevant to model prediction variability. Furthermore, the SGS approach is advantageous for high-dimensional models (multiple parameters).

The SGS approach calculates the Sobol sensitivity indices using analysis of variance (ANOVA) decomposition, as indicated by Equations (34) and (35) below:

$$D_{i_1 \ldots i_s} = \int_0^1 f^2_{i_1 \ldots i_s}\, dx_{i_1} \ldots dx_{i_s} \tag{34}$$

$$D = \int_0^1 f^2(x)\, dx - f_o^2 = \sum_{s=1}^{n} \sum_{i_1 < \ldots < i_s} D_{i_1 \ldots i_s} \tag{35}$$

where f(x) is an integrable function of a given model parametrization, with $f(x) \in \mathbb{R}$ and $x \in \mathbb{R}^n$; x_{i_1} to x_{i_s} are the predictors of the function f(x); $D_{i_1 \ldots i_s}$ is the variance associated with a given model parameter; D is the total variance observed; and f_o is a generic initial value of function f(x).

The Sobol global sensitivity index is calculated as the ratio between the variances, as indicated by Equation (36):

$$S_{i_1 \ldots i_s} = \frac{\int_0^1 f^2_{i_1 \ldots i_s}\, dx_{i_1} \ldots dx_{i_s}}{\sum_{s=1}^{n} \sum_{i_1 < \ldots < i_s} D_{i_1 \ldots i_s}} \tag{36}$$

where $S_{i_1 \ldots i_s}$ means the Sobol global sensitivity index for each parameter of a given mathematical model.

In this study, the Global Sensitivity Analysis Toolbox (GSAT) for MATLAB developed by [96] was used to calculate the Sobol global sensitivity indices for the spatial k_p novel model, as indicated in its complete form by Equation (37), and the $NDVI_{soil}$ and $NDVI_c$ novel approaches (Equations (10) and (11), respectively).

$$k_p = \beta_o + \beta_1 \left(\frac{1}{LAI} \right) \times \ln \left(\frac{NDVI - NDVI_c}{NDVI_{soil} - NDVI_c} \right) \tag{37}$$

For the SGS analysis, the four input parameters in Equation (37) are LAI, NDVI, $NDVI_c$, and $NDVI_{soil}$ since β_o and β_1 are fixed regression coefficients when statistically relating k_p and k_v. Regarding the SGS analysis of $NDVI_{soil}$ and $NDVI_c$ models, there are three input parameters: NDVI, f_c, and $d(NDVI)/df_c$. The parameters with higher Sobol global sensitivity indices are the ones that have more influence on model variability and accuracy [96]. For more details on how to access the GSAT for MATLAB package and intrinsic information about the SGS approach, refer to [96].

3. Results

3.1. The Error Analysis of f_c, LAI, $NDVI_{soil}$, and $NDVI_c$

When assessing the performance of f_c [31,32] and LAI [65] models in this study, it is evident that both models provided canopy architecture predictions that were in good agreement with observed values of their respective variables (Figure 5). For the case of f_c, the error was 0.02 (2%) ± 0.07 (10%), with the f_c model explaining 53% of the variability observed in the indirect measurements of f_c using the PAR sensors. Similar performance was observed from the LAI model, with an error of 0.08 m^2/m^2 (3%) ± 0.36 m^2/m^2 (11%). However, the LAI model was able to explain more of the variability in the observed LAI dataset (R^2 of 0.87) compared to the f_c model performance. Both f_c and LAI models somewhat overestimated their respective predictions of maize canopy architecture in this study. However, the overestimation was minor in magnitude (2% for f_c and 3% for LAI predictions). Since LAI is an input in the f_c model, it is clear that part of the overestimation in f_c is primarily due to the LAI overestimation.

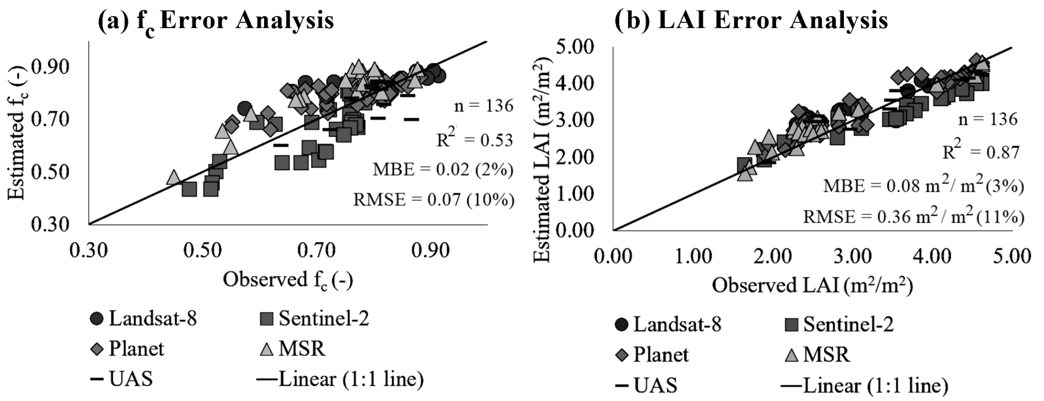

Figure 5. Scatter plots of observed f_c vs. estimated f_c (**a**) and the observed LAI vs. the estimated LAI (**b**) with the error analysis statistics. LIRF 2018 and 2022 datasets.

When considering the performance of each LAI and f_c model per RS sensor, the NRMSE values for LAI prediction ranged from 9% (UAS) to 13% (Sentinel-2). There was only an underestimation of the LAI when using the Sentinel-2 multispectral data as an input (−4%). Clearly, the underestimation of the LAI due to Sentinel-2 was not significant enough to cause an overall underestimation of the LAI when combining all the RS sensor data in the analysis (Table 1). The most considerable overestimation of the LAI was obtained from the MSR multispectral sensor (8%), which could be associated with induced systematic errors in the data collection process, given the nature of the measurements being manually performed in the field by different individuals due to field work logistics. The lowest overestimation of LAI predictions was observed when the UAS data were used as inputs (1%). Given the fine spatial scale of the UAS multispectral imagery data (<0.10 m), the assessment of point-based conditions seemed more adequate compared to larger spatial scale RS sensors in this study. The explained variability in the LAI data ranged from 84% (Landsat-8) to 93% (MSR).

Table 1. The error analysis of the LAI across each of the RS sensors in the study. LIRF 2018 and 2022 datasets combined.

	n	MBE (NMBE)	RMSE (NRMSE)	R^2
Landsat-8	16	0.20 (6%)	0.39 (12%)	0.84
Sentinel-2	34	−0.11 (−4%)	0.43 (13%)	0.88
Planet CubeSat	49	0.13 (4%)	0.33 (10%)	0.91
MSR	24	0.22 (8%)	0.33 (12%)	0.93
UAS	13	0.03 (1%)	0.31 (9%)	0.89

The error analysis of f_c predictions across each RS sensor indicated that the NRMSE ranged from 8% (UAS) to 11% (Sentinel-2), which presented the same RS sensors as the lowest and highest NRMSE compared to the LAI model assessment. Regarding the underestimation or overestimation of f_c, underestimation of f_c was observed when using Sentinel-2 and UAS multispectral data as inputs to predict f_c (Table 2). The underestimation of f_c from Sentinel-2 data (−6%) can be related to the underestimation of the LAI when using the same RS sensor data (−4%) since the LAI is an input to estimate f_c in this study. Surprisingly enough, the same pattern is not observed regarding the UAS multispectral data. For the UAS, there was a slight overestimation of the LAI (1%), while f_c predictions were underestimated (−3%). Given the spatial scale nature of UAS imagery (<0.10 m) and the fact that the f_c models from [31,32] introduce the concept of a vegetation clumping factor, it is expected that the clumping factor calculations may not completely represent the vegetated point-based conditions observed in the UAS data, which could contribute to an overestimation of f_c values.

Table 2. The error analysis of f_c across the different RS sensors in the study. LIRF 2018 and 2022 datasets combined.

	n	**MBE (NBME)**	**RMSE (NRMSE)**	**R^2**
Landsat-8	16	0.04 (5%)	0.08 (10%)	0.40
Sentinel-2	34	−0.04 (−6%)	0.08 (11%)	0.64
Planet CubeSat	49	0.03 (4%)	0.07 (9%)	0.49
MSR	24	0.07 (10%)	0.08 (11%)	0.84
UAS	13	−0.03 (−3%)	0.07 (8%)	0.38

Regarding the analysis of $NDVI_c$ and $NDVI_{soil}$ predictions using the novel approaches derived in this study, there were smaller errors associated with $NDVI_c$ compared to $NDVI_{soil}$ predictions (Figure 6). The $NDVI_c$ estimation had an error of −0.01 (−2%) ± 0.07 (9%). In comparison, the $NDVI_{soil}$ error was 0.01 (3%) ± 0.02 (17%). The larger NRMSE associated with $NDVI_{soil}$ could be due to the fact that the $NDVI_{soil}$ model uses NDVI as an input and that the mean value of observed $NDVI_{soil}$ (0.144) is significantly lower than the mean observed $NDVI_c$ value (0.842). NDVI values change significantly over time since plants' seasonal growth is not a linear process. However, given that the dry soil surface reflectance responses over time do not change significantly, it is evident that the predictions of NDV_{soil} differ from the most constant values of NDVI observed for bare soil parts of the maize fields at the LIRF in 2018 and 2022. Now, given that $NDVI_c$ theoretically varies more as the plants grow and increase their green foliage through time and space, it is expected that the $NDVI_c$ model should agree more with on-site values of NDVI for plants.

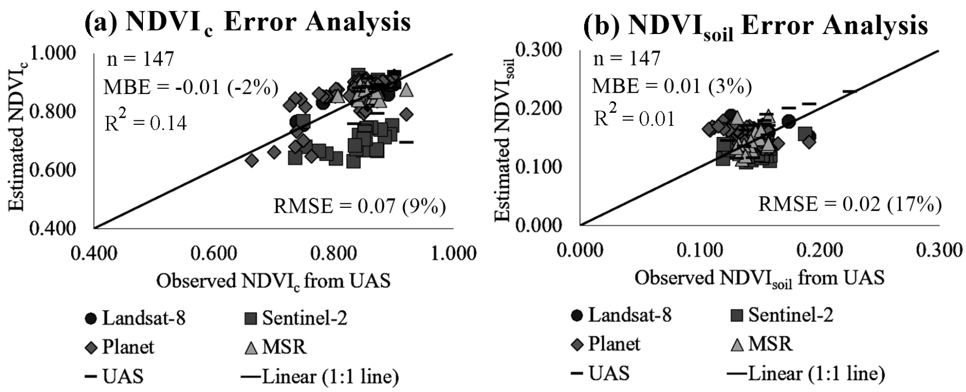

Figure 6. Scatter plots of observed $NDVI_c$ vs. estimated $NDVI_c$ (**a**) and observed $NDVI_{soil}$ vs. estimated $NDVI_{soil}$ (**b**) with the error analysis statistics. LIRF 2018 and 2022 datasets.

3.2. *The Novel k_p Model Regression Results*

The calibration of the k_p model (Equation (37)) using LIRF 2020 and IIC 2020–2021 datasets provided the following calibrated equation (Table 3) for predicting spatial k_p (Equation (38)) for maize, with an R^2 of 0.95:

$$k_p = -0.05 + 0.78 \times \left(\frac{1}{LAI}\right) \times \ln\left(\frac{NDVI - NDVI_c}{NDVI_{soil} - NDVI_c}\right) \quad (38)$$

Table 3. The summary statistics * of the k_p regression model using LIRF 2020 and IIC 2020–2021 datasets combining data from all RS sensors in this study.

	Estimate	95% Confidence Interval	Standard Error	Test Statistic	*p*-Value
Intercept (β_o)	−0.05	[−0.06, −0.03]	0.01	−5.19	5.23×10^{-7}
Slope (β_1)	0.78	[0.76, 0.81]	0.01	61.988	2.82×10^{-130}

* Number of observations: 197; Error degrees of freedom: 195; RMSE: 0.02; F-statistic: 3.84×10^3.

The calibrated k_p model accounts for 95% of the variability observed in the k_p data, which is a good indication that the developed model has a strong and positive statistical linear relationship between k_p and k_v (Figure 7), as observed in the literature [36]. The intercept and slope regression coefficients have a 95% confidence interval ranging from −0.06 to −0.03 and 0.76 to 0.81, respectively. The *p*-values are statistically significant (<5%), which indicates that the regressed coefficient estimates are statistically validated for future model predictions.

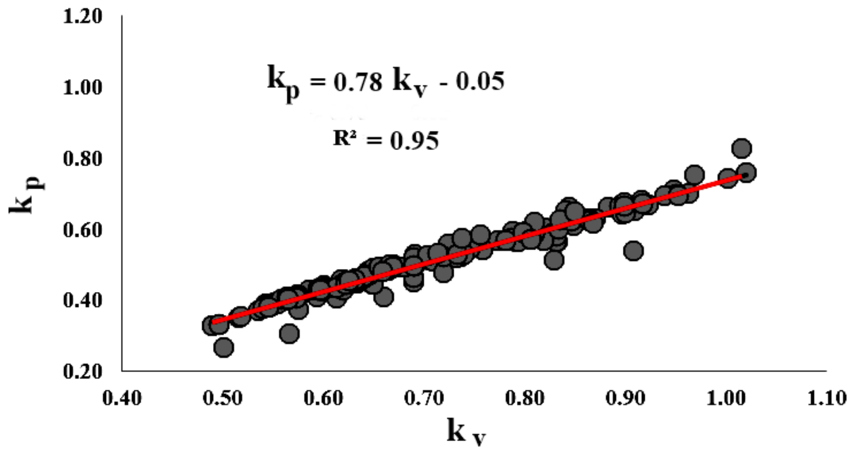

Figure 7. The fitted k_p model considering LIRF 2020 and IIC 2020–2021 datasets across all remote sensors in this study.

When resorting to the analysis of the individual model regression product per RS sensor (e.g., spaceborne, proximal, airborne), similar results were obtained as compared to the fully regressed model combining all RS datasets for the LIRF and IIC 2020 and 2021 data (Figure 8). When comparing the regressed intercept estimation per RS sensor, the values were within the range of −0.03 to −0.08. Planet CubeSat and the MSR had the same intercept value (−0.03). Similarly, Landsat-8 and UAS had a model intercept of −0.08. Only Sentinel-2 had a different intercept value (−0.05) compared to the remaining RS sensor.

All the regressed intercepts were statistically significant (*p*-value < 0.05), as indicated in Table 4. Regarding the regressed slopes, the estimated values varied from 0.76 to 0.84. Landsat-8 had the same slope as the UAS. The remaining remote sensors had slopes ranging from 0.76 to 0.79. With the exception of Landsat-8, all the regressed slopes were statistically significant. Regarding the fitted R^2, all RS platforms had very strong and positive R^2 values (Table 4), with the lowest being Planet CubeSat (R^2 = 0.93) and the highest being the MSR (R^2 = 0.99). Given that the combined calibration of the k_p model using data from all the RS sensors (Equation (37)) presents a more robust statistical analysis since the sample size is large enough to support the validation of the model (n = 197), we suggest that its regressed coefficients should be used when predicting k_p.

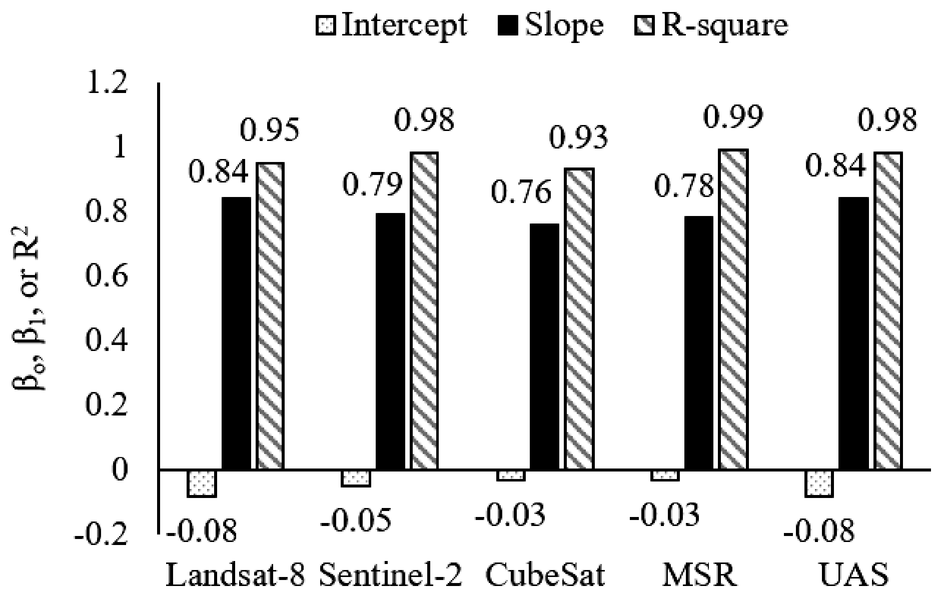

Figure 8. The fitted k_p model parameters considering LIRF 2020 and IIC 2020–2021 datasets across all RS sensors in this study.

Table 4. The summary statistics of the k_p regression model using LIRF 2020 and IIC 2020–2021 datasets for RS sensors in this study.

	n	R^2	Regressed Coefficients	Estimate	95% Confidence Interval	Standard Error	Test Statistic	*p*-Value
Landsat-8	16	0.95	Intercept (β_o)	−0.08	[−0.17, 0.01]	0.04	−1.95	8.00×10^{-3}
			Slope (β_1)	0.84	[0.71, 0.95]	0.05	15.38	0.95
Sentinel-2	31	0.98	Intercept (β_o)	−0.05	[−0.07, −0.02]	0.01	−3.52	1.45×10^{-3}
			Slope (β_1)	0.79	[0.75, 0.83]	0.02	40.89	3.40×10^{-27}
Planet CubeSat	90	0.93	Intercept (β_o)	−0.03	[−0.07, 0.01]	0.02	−2.27	0.03
			Slope (β_1)	0.76	[0.72, 0.81]	0.02	34.63	4.79×10^{-53}
MSR	39	0.99	Intercept (β_o)	−0.03	[−0.05, −0.02]	0.01	−3.74	6.16×10^{-4}
			Slope (β_1)	0.78	[0.75, 0.81]	0.01	52.66	2.12×10^{-36}
UAS	21	0.98	Intercept (β_o)	−0.08	[−0.12, −0.04]	0.02	−3.96	8.32×10^{-4}
			Slope (β_1)	0.84	[0.78, 0.90]	0.03	30.83	1.09×10^{-17}

When calculating the $\frac{d}{df_c}(\mathrm{NDVI})$ term (Equation (12)) in Equation (37), the linear regression between the minimum and maximum NDVI and respective measured f_c values (Figure 9 and Table 5) provided the two distinct values of $\frac{d}{df_c}(\mathrm{NDVI}_{min})$ and $\frac{d}{df_c}(\mathrm{NDVI}_{max})$ for the linear interpolation to determine any $\frac{d}{df_c}(\mathrm{NDVI})$ for any given f_c between 0 and 0.85. The respective calculated values for $\frac{d}{df_c}(\mathrm{NDVI}_{min})$ and $\frac{d}{df_c}(\mathrm{NDVI}_{max})$ were 0.25 (f_c = 0) and 0.39 (f_c = 0.85). These results are $\frac{d}{df_c}(\mathrm{NDVI}_{min})$ less than $\frac{d}{df_c}(\mathrm{NDVI}_{max})$ since the linear regression slopes for each case scenario (minimum and maximum NDVI groups) are proportional to the magnitude of NDVI values used for the regression approach.

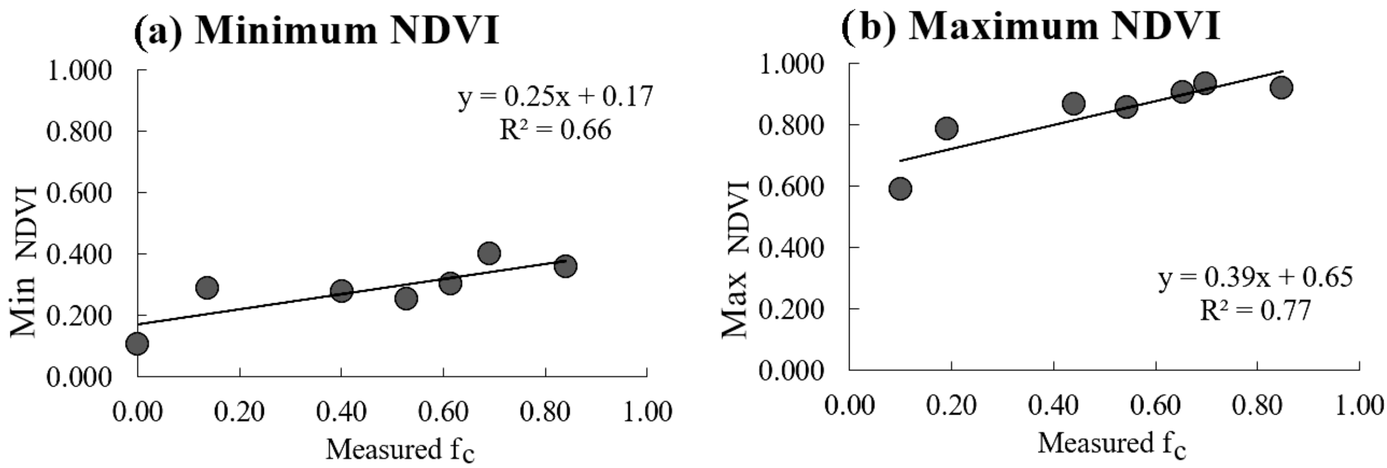

Figure 9. Scatter plots of the calculations regarding $\frac{d}{df_c}(NDVI_{min})$ and $\frac{d}{df_c}(NDVI_{max})$ values.

Table 5. The data to determine minimum and maximum $d(NDVI)/df_c$ values. Data included all RS sensors in this study from LIRF 2020, IIC 2020, and 2021 datasets.

Measured f_c	f_c Value	Min NDVI	f_c Value	Max NDVI
$f_c < 0.10$	0	0.106	0.10	0.590
$0.10 < f_c \leq 0.35$	0.14	0.289	0.19	0.788
$0.35 < f_c \leq 0.45$	0.40	0.277	0.44	0.868
$0.45 < f_c \leq 0.55$	0.53	0.253	0.54	0.857
$0.55 < f_c \leq 0.65$	0.61	0.301	0.65	0.907
$0.65 < f_c \leq 0.75$	0.69	0.399	0.70	0.933
$0.75 < f_c \leq 0.85$	0.84	0.358	0.85	0.921

3.3. Accuracy Comparison between the Novel k_p and [27] Models

When comparing the proposed k_p model with the original and simplified [27] k_p approaches, it was evident that the novel k_p model (Equation (38)) outperformed the other two approaches (Figure 10 and Table 6). For the case scenario combining all RS sensor data into the error analysis, the overall error (MBE ± RMSE) in predicting k_p using the novel approach was −0.01 (−2%) ± 0.05 (10%), a 44% improvement compared to the original and simplified models, with a k_p prediction error of 0.07 (14%) ± 0.09 (18%) for both. There was a slight underestimation of k_p in the novel approach (−2%), which is due to the fact that the calibrated model (Equation (38)) does not characterize the entire variability in observed k_p values. A considerable overestimation of k_p values was part of the [27] models (14%). Ref. [27] assumes a theoretical foliage shape that is often violated within field conditions. Also, the inherited assumptions concerning the ratio of horizontal and vertical leaf lengths add extra uncertainty when predicting k_p since it is hard to model, and there is spatial and local variability from plant to plant within an agricultural field.

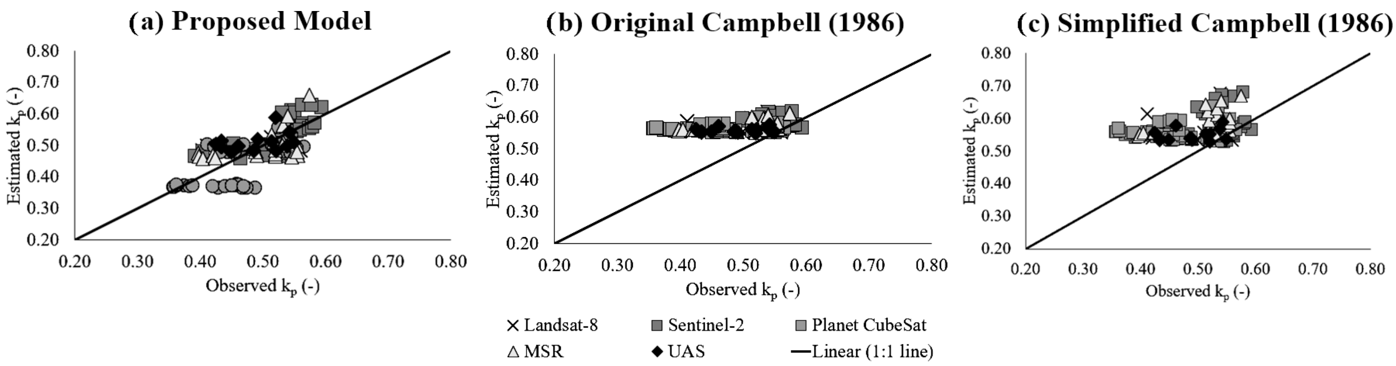

Figure 10. Scatter plots of observed k_p vs. estimated k_p regarding the novel k_p approach (**a**), the original [27] k_p model (**b**), and the simplified [27] k_p model (**c**). This analysis involved LIRF 2018 and 2022 datasets.

Table 6. The error analysis statistics regarding the comparison between observed and estimated k_p for the novel, original [27], and simplified [27] approaches. LIRF 2018 and 2022 data combined.

	Proposed and Novel k_p Model	Original [27] k_p Model	Simplified [27] k_p Model
N	136	136	136
MBE (-)	−0.01	0.07	0.07
NMBE (%)	−2%	14%	14%
RMSE (-)	0.05	0.09	0.09
NRMSE (%)	10%	18%	18%
R^2	0.56	0.27	0.22

The novel k_p approach (Equation (38)) seemed to better represent the temporal variability in k_p values compared to the [27] approaches (Figure 10). The pair of points (observed k_p, estimated k_p) from the novel approach was scattered around the 1:1 line (Figure 10a). The same pattern was not observed for the [27] k_p model (Figure 10b,c) cases. Since the original and simplified k_p models do not account for local field conditions in their approach, the temporal variability due to changes in the actual canopy architecture is not entirely addressed by the models. The assumption of the leaf distribution parameter being a constant value does not allow for the incorporation of the actual field conditions regarding the canopy foliage arrangement over time. Thus, the [27] approaches had a small R^2 (<0.30), while the novel k_p approach was able to explain more of the variability observed in k_p (R^2 of 0.56) during the independent data validation phase (LIRF 2018 and 2022 datasets).

When analyzing the performance of each k_p approach in this study per RS sensor, it was evident that consistent results were observed regarding the better performance of the novel k_p model compared to the [27] approaches (Figure 11). The NRMSE values for the novel k_p approach (Equation (38)) ranged from 8% (Sentinel-2) to 12% (Planet CubeSat), with an evident underestimation of k_p estimated values when using Landsat-8 (−3%), Planet CubeSat (−6%), and MSR (−1%) multispectral data as inputs to predict k_p. Regardless of the [27] approach, there was a high overestimation of estimated k_p values, with NMBE ranging from 8% to 19%.

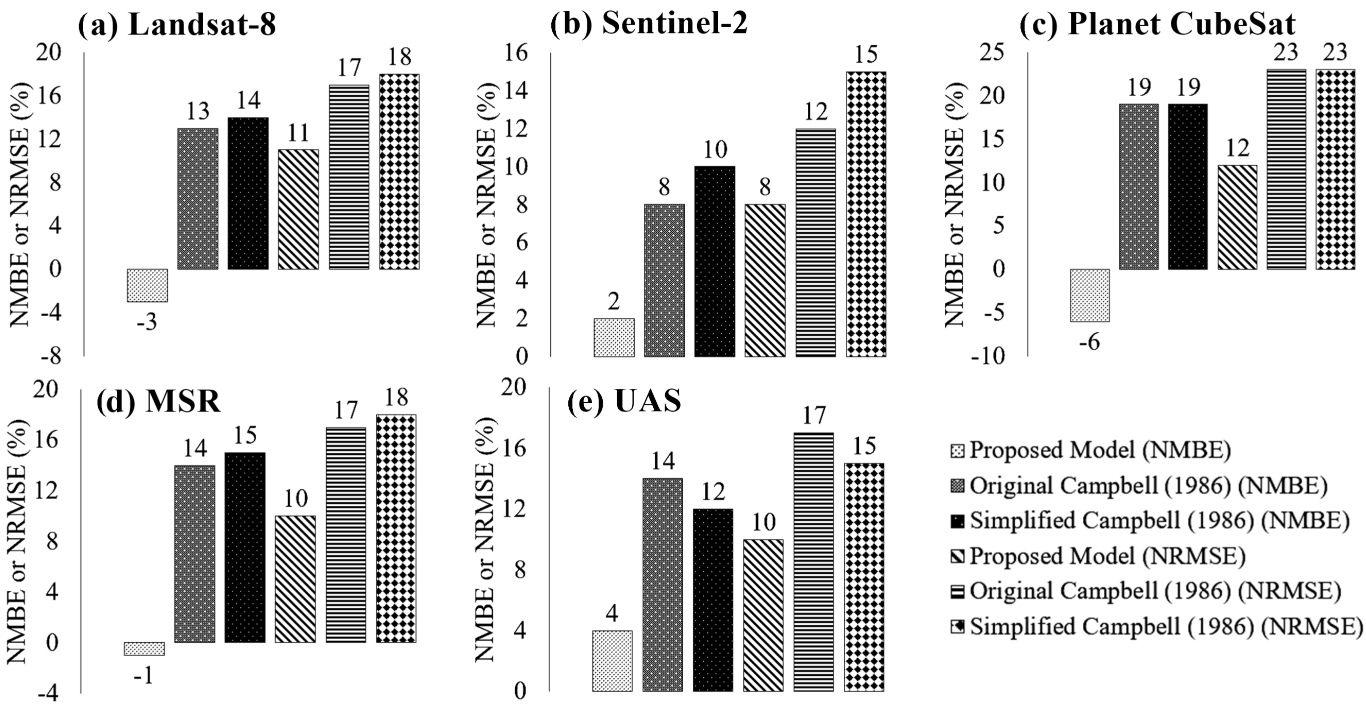

Figure 11. Bar plots for the NBME and NRMSE of estimated k_p values for each remote sensor. This analysis involved LIRF 2018 and 2022 datasets.

3.4. The Global Sensitivity Analysis of the k_p, $NDVI_{soil}$, and $NDVI_c$ Model Variables

The SGS analysis of the k_p model indicated that NDVI is the primary variable that accounts for most of the variability in the predictions of k_p since it had the highest Sobol index compared to the other variables in the model across the RS sensors (Figure 12). The Sobol index for NDVI varied from 0.54 (Sentinel-2) to 0.67 (Landsat-8). The other inputs (the LAI, $NDVI_c$, and $NDVI_{soil}$) have lower Sobol indices (<0.30), which indicates that those input variables have less accountability for the accuracy of k_p predictions. When evaluating the $NDVI_c$ and $NDVI_{soil}$ models, the NDVI input variable was also more relevant in explaining the variability observed in partitioning NDVI values in canopy and soil composites (Table 7). The Sobol index for the NDVI variable ranged from 0.88 to 0.94 regarding the $NDVI_c$ model and from 0.55 to 0.64 regarding the $NDVI_{soil}$ approach.

Table 7. The Sobol global sensitivity indices for the novel $NDVI_c$ and $NDVI_{soil}$ models.

		Sobol Global Sensitivity Index		
Model	**Remote Sensor**	**NDVI**	$\mathbf{f_c}$	$\frac{d}{df_c}$(**NDVI**)
$NDVI_c$	Landsat-8	0.88	0.12	0
	Sentinel-2	0.93	0.06	0.01
	Planet CubeSat	0.90	0.09	0.01
	MSR	0.91	0.09	0
	UAS	0.94	0.06	0
$NDVI_{soil}$	Landsat-8	0.55	0.40	0.04
	Sentinel-2	0.64	0.33	0.03
	Planet CubeSat	0.58	0.38	0.04
	MSR	0.58	0.38	0.04
	UAS	0.60	0.36	0.04

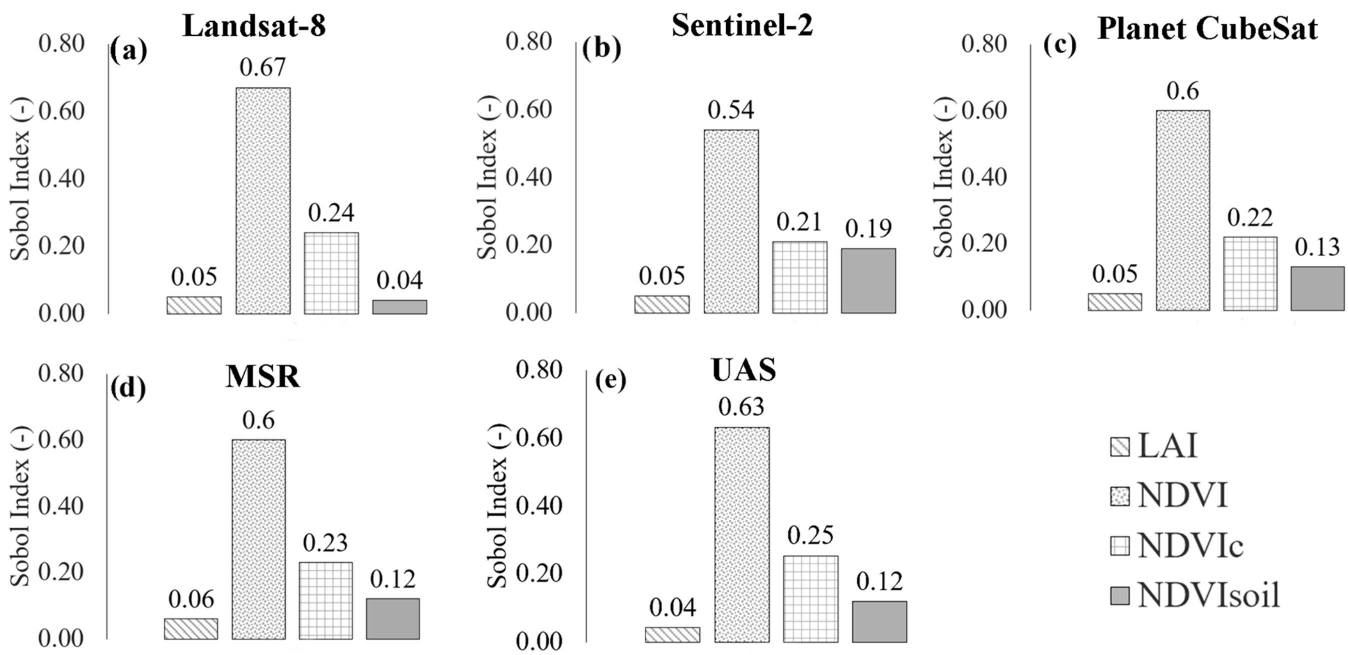

Figure 12. Bar plots of observed Sobol global sensitivity indices for the novel k_p model.

Regardless of the NDVI composite model for canopy and bare soil, the $\frac{d}{df_c}$(NDVI) input variable had a negligible contribution to explaining the variance in k_p predictions (Sobol indices near zero). Since the total sum of all the Sobol indices for a given model is equal to one, it is evident that there were differences in how relevant f_c is for either $NDVI_c$ or $NDVI_{soil}$. When looking at the Sobol indices for f_c only, the $NDVI_c$ model had lower Sobol index values for f_c compared to the $NDVI_{soil}$ Sobol index values for the same input (Table 7). That is, the f_c input variable is more important to explain the variability in $NDVI_{soil}$ prediction than to $NDVI_c$.

One reason to justify this research finding is the apparent connection between NDVI and $NDVI_c$. For nearly fully grown vegetated surfaces, NDVI and $NDVI_c$ values are alike since there is little bare soil exposure due to leaves covering most of the ground surface. Thus, most of the variability in $NDVI_c$ can be explained by NDVI values under those conditions, which leads to a small contribution to the $NDVI_c$ variance from f_c in the proposed novel $NDVI_c$ model. For the $NDVI_{soil}$ model, the predictions are associated with NDVI values during the same crop growing season, which means that the estimation of $NDVI_{soil}$ is for conditions that are also associated with plants entering the complete canopy growth stages. In that case, NDVI values are at their maximum while the $NDVI_{soil}$ must remain nearly constant within root zone wetting periods (e.g., irrigation or rainfall events). Thus, the f_c input variable tends to be more important for explaining the variance in $NDVI_{soil}$ estimation than for $NDVI_c$ model predictions. Nonetheless, it is essential to emphasize that $NDVI_{soil}$ and $NDVI_c$ prediction variances are mainly dependent on NDVI, given that that was the input variable with the highest Sobol index in both NDVI composite models (Table 7).

4. Conclusions

In this study, the calibration of the k_p model resulted in the development of a robust predictive model for an RS-based spatial k_p characterization. The k_p model, determined with a regression coefficient of determination R^2 value of 0.95, demonstrated a strong statistical linear relationship between k_p and k_v. The regression coefficients, including the intercept and slope, exhibited 95% confidence intervals and *p*-values that seem to validate the k_p model's reliability for future predictions. The k_p model performance analysis considered maize surface multispectral data from several RS sensors, revealing consistent statistical results across the various sensors investigated. Although slight variations existed in intercept and slope values, for the k_p model, among the RS sensors, all platforms exhibited strong R^2 values, which emphasizes the novel k_p model's consistent performance.

A model performance comparison with the k_p models by [27] highlighted the advantages of using the proposed k_p model to considerably improve the spatial k_p estimation accuracy. An overall 44% improvement in accuracy was observed when using the novel k_p model compared to the [27] models. The novel k_p approach not only outperformed the classic k_p models but also captured temporal variability more effectively, which highlights its applicability in dynamic environmental conditions. A global sensitivity analysis showed the significance of NDVI in predicting k_p across the different remote sensors investigated, with f_c playing a more crucial role in $NDVI_{soil}$ predictions than in $NDVI_c$.

While the study provides insights into model performance, future research directions should focus on addressing observed underestimations and variations in specific sensors due to their spectral and spatial differences. Since the importance of sensor-specific characteristics is critical to address the quality of data inputs for modeling environmental variables, the use and application of the calibrated and novel k_p model must be interpreted with care, given the nature of the calibration process and data collection used in this research. For a more robust validation, more research must be performed regarding other valuable row crops under different climate zones to evaluate any potential differences in the calibration coefficients. Also, incorporating more RS sensors at a much larger spatial scale might provide the conditions to use the novel k_p model for large-scale modeling (e.g., watershed). Therefore, the continuous refinement and validation of the k_p model using diverse datasets and additional sensors will further enhance its applicability to different local field conditions and provide the means to expand the use of this novel k_p model for a wide range of environmental applications.

Author Contributions: E.C.-F. processed the data, conducted the statistical analysis, and wrote the bulk of the manuscript; J.L.C. obtained financial and logistic support and guided the research efforts, was involved in the article editing; and H.Z. was involved in fieldwork planning, unmanned aerial system management, manuscript formatting, and writing adjustments. All authors have read and agreed to the published version of the manuscript.

Funding: This research was funded by the Irrigation Innovation Consortium (IIC), Northern Colorado Water Conservancy District (Northern Water), and the Colorado Agricultural Experiment Station (CAES)—USDA NIFA project grant number COL00796.

Data Availability Statement: The data that supported the findings of this study are available from the corresponding author upon reasonable request.

Acknowledgments: We would like to thank Cole Lucero, Rustin Jensen, Mia Morones, Kelsey Walker, Jon Altenhofen, Katie Ascough, Brianna Trotter, Alex Olsen, Kevin Yemoto, Ross Steward, Garrett Banks, and Luke Stark for the field efforts to collect data, install instrumentation, and manage farm management activities—special thanks to Ansley Brown and Allan Andales for helping with the research logistics at the IIC site.

Conflicts of Interest: The authors declare that they do not have any conflict of interest, as well as no competing financial interests or personal relationships that could have appeared to influence the contents of this study.

References

1. Arthur, J.M. Some effects of radiant energy on plants. *JOSA* **1929**, *18*, 253–263. [CrossRef]
2. Chavez, J.C.; Ganjegunte, G.K.; Jeong, J.; Rajan, N.; Zapata, S.D.; Ruiz-Alvarez, O.; Enciso, J. Radiation Use Efficiency and Agronomic Performance of Biomass Sorghum under Different Sowing Dates. *Agronomy* **2022**, *12*, 1252. [CrossRef]
3. Gallo, K.P.; Daughtry, C.S.T. Techniques for measuring intercepted and absorbed Photosynthetically Active Radiation in Corn Canopies 1. *Agron. J.* **1986**, *78*, 752–756. [CrossRef]
4. Gitelson, A.A.; Peng, Y.; Arkebauer, T.J.; Suyker, A.E. Productivity, absorbed photosynthetically active radiation, and light use efficiency in crops: Implications for remote sensing of crop primary production. *J. Plant Physiol.* **2015**, *177*, 100–109. [CrossRef] [PubMed]
5. Kudrjavceva, A.A. Reflection, absorption and penetration of solar radiation in relation to the stand of agricultural plants. *Dokl. Vsesoyuznoi Akad. Sel'sko-Khozyaistvennykh Nauk Im VI Lenina* **1940**, *2*, 11–15.

6. Raschke, K. Heat transfer between the plant and the environment. *Annu. Rev. Plant Physiol.* **1960**, *11*, 111–126. [CrossRef]
7. Thimann, K.V. *Biological Utilization of Solar Energy*; American Academy of Arts & Sciences: Cambridge, MA, USA, 1951; Volume 79, pp. 323–326.
8. Ross, J. *The Radiation Regime and Architecture of Plant Stands*; (No. 3); Springer Science & Business Media: Berlin/Heidelberg, Germany, 1981.
9. Weiss, M.; Baret, F.; Smith, G.J.; Jonckheere, I.; Coppin, P. Review of methods for in situ leaf area index (LAI) determination: Part II. Estimation of LAI, errors and sampling. *Agric. For. Meteorol.* **2004**, *121*, 37–53. [CrossRef]
10. Carlson, T.N.; Ripley, D.A. On the relation between NDVI, fractional vegetation cover, and leaf area index. *Remote Sens. Environ.* **1997**, *62*, 241–252. [CrossRef]
11. Lalic, B.; Mihailovic, D.T. An empirical relation describing leaf-area density inside the forest for environmental modeling. *J. Appl. Meteorol.* **2004**, *43*, 641–645. [CrossRef]
12. Murchie, E.H.; Burgess, A.J. Casting light on the architecture of crop yield. *Crop Environ.* **2022**, *1*, 74–85. [CrossRef]
13. Reta-Sánchez, D.G.; Fowler, J.L. Canopy light environment and yield of narrow-row cotton as affected by canopy architecture. *Agron. J.* **2002**, *94*, 1317–1323. [CrossRef]
14. Walcroft, A.S.; Brown, K.J.; Schuster, W.S.; Tissue, D.T.; Turnbull, M.H.; Griffin, K.L.; Whitehead, D. Radiative transfer and carbon assimilation in relation to canopy architecture, foliage area distribution and clumping in a mature temperate rainforest canopy in New Zealand. *Agric. For. Meteorol.* **2005**, *135*, 326–339. [CrossRef]
15. Tang, L.; Yin, D.; Chen, C.; Yu, D.; Han, W. Optimal design of plant canopy based on light interception: A case study with loquat. *Front. Plant Sci.* **2019**, *10*, 364. [CrossRef] [PubMed]
16. Banerjee, T.; Linn, R. Effect of vertical canopy architecture on transpiration, thermoregulation, and carbon assimilation. *Forests* **2018**, *9*, 198. [CrossRef]
17. Buler, Z.; Mika, A. The influence of canopy architecture on light interception and distribution in 'Sampion'apple trees. *J. Fruit Ornaments Plant Res.* **2009**, *17*, 45–52.
18. Gao, Y.; Gao, S.; Jia, L.; Dai, T.; Wei, X.; Duan, J.; Liu, S.; Weng, X. Canopy characteristics and light distribution in *Sapindus mukorossi* Gaertn. are influenced by crown architecture manipulation in the hilly terrain of Southeast China. *Sci. Hortic.* **2018**, *240*, 11–22. [CrossRef]
19. Ratikanta, M.; Gonzalez, R.H.; NS, K.T.; KalamosIsland, L. Variability in leaf canopy architecture may be related to photosynthetic efficiency and carbon fixation. *Int. J. Bio-Resour. Stress Manag.* **2014**, *5*, i–ii.
20. Campbell, G.S.; Norman, J.M. The light environment of plant canopies. In *An Introduction to Environmental Biophysics*; Springer: New York, NY, USA, 1998; pp. 247–278.
21. Monteith, J.L. Light interception and radiative exchange in crop stands. *Physiol. Asp. Crop Yield* **1969**, 89–111. [CrossRef]
22. Anderson, M.C. Stand structure and light penetration. II. A theoretical analysis. *J. Appl. Ecol.* **1966**, *3*, 41–54. [CrossRef]
23. Marshall, J.D.; Waring, R.H. Comparison of methods of estimating leaf-area index in old-growth Douglas-fir. *Ecology* **1986**, *67*, 975–979. [CrossRef]
24. Monsi, M.; Saeki, T. The light factor in plant communities and its significance for dry matter production. *Jpn. J. Bot.* **1953**, *14*, 22–52.
25. Nilson, T. A theoretical analysis of the frequency of gaps in plant stands. *Agric. Meteorol.* **1971**, *8*, 25–38. [CrossRef]
26. Gao, L.; Wang, X.; Johnson, B.A.; Tian, Q.; Wang, Y.; Verrelst, J.; Mu, X.; Gu, X. Remote sensing algorithms for estimation of fractional vegetation cover using pure vegetation index values: A review. *ISPRS J. Photogramm. Remote Sens.* **2020**, *159*, 364–377. [CrossRef] [PubMed]
27. Campbell, G.S. Extinction coefficients for radiation in plant canopies calculated using an ellipsoidal inclination angle distribution. *Agric. For. Meteorol.* **1986**, *36*, 317–321. [CrossRef]
28. Ruimy, A.; Kergoat, L.; Bondeau, A.; The Participants of the Potsdam NPP Model Intercomparison. Comparing global models of terrestrial net primary productivity (NPP): Analysis of differences in light absorption and light-use efficiency. *Glob. Chang. Biol.* **1999**, *5*, 56–64. [CrossRef]
29. Waring, R.H.; Coops, N.C.; Mathys, A.; Hilker, T.; Latta, G. Process-based modeling to assess the effects of recent climatic variation on site productivity and forest function across western North America. *Forests* **2014**, *5*, 518–534. [CrossRef]
30. Colaizzi, P.D.; Kustas, W.P.; Anderson, M.C.; Agam, N.; Tolk, J.A.; Evett, S.R.; Howell, T.A.; Gowda, P.H.; O'shaughnessy, S.A. Two-source energy balance model estimates of evapotranspiration using component and composite surface temperatures. *Adv. Water Resour.* **2012**, *50*, 134–151. [CrossRef]
31. Kustas, W.P.; Norman, J.M. A Two-Source Energy Balance Approach Using Directional Radiometric Temperature Observations for Sparse Canopy Covered Surfaces. *Agron. J.* **2000**, *92*, 847–854. [CrossRef]
32. Norman, J.M.; Kustas, W.P.; Humes, K.S. Source approach for estimating soil and vegetation energy fluxes in observations of directional radiometric surface temperature. *Agric. For. Meteorol.* **1995**, *77*, 263–293. [CrossRef]
33. Tahiri, A.Z.; Anyoji, H.; Yasuda, H. Fixed and variable light extinction coefficients for estimating plant transpiration and soil evaporation under irrigated maize. *Agric. Water Manag.* **2006**, *84*, 186–192. [CrossRef]
34. Zhang, L.; Hu, Z.; Fan, J.; Zhou, D.; Tang, F. A meta-analysis of the canopy light extinction coefficient in terrestrial ecosystems. *Front. Earth Sci.* **2014**, *8*, 599–609. [CrossRef]

35. Goudriaan, J.; Van Laar, H.H. *Modelling Potential Crop Growth Processes. Current Issues in Production Ecology*; Kluwer Academic Publishers: Norwell, MA, USA, 1994; Volume 10, pp. 978–994.
36. Baret, F.; Clevers, J.G.P.W.; Steven, M.D. The robustness of canopy gap fraction estimates from red and near-infrared reflectances: A comparison of approaches. *Remote Sens. Environ.* **1995**, *54*, 141–151. [CrossRef]
37. Choudhury, B.J.; Ahmed, N.U.; Idso, S.B.; Reginato, R.J.; Daughtry, C.S. Relations between evaporation coefficients and vegetation indices studied by model simulations. *Remote Sens. Environ.* **1994**, *50*, 1–17. [CrossRef]
38. Price, J.C. Estimating vegetation amount from visible and near infrared reflectances. *Remote Sens. Environ.* **1992**, *41*, 29–34. [CrossRef]
39. Price, J.C.; Bausch, W.C. Leaf area index estimation from visible and near-infrared reflectance data. *Remote Sens. Environ.* **1995**, *52*, 55–65. [CrossRef]
40. Jones, H.G. *Plants and Microclimate: A Quantitative Approach to Environmental Plant Physiology*; Cambridge University Press: Cambridge, UK, 2013.
41. Ranum, P.; Peña-Rosas, J.P.; Garcia-Casal, M.N. Global maize production, utilization, and consumption. *Ann. N. Y. Acad. Sci.* **2014**, *1312*, 105–112. [CrossRef]
42. Allen, L.H.; Yocum, C.S.; Lemon, E.R. Photosynthesis Under Field Conditions. VII. Radiant Energy Exchanges Within a Corn Crop Canopy and Implications in Water Use Efficiency 1. *Agron. J.* **1964**, *56*, 253–259. [CrossRef]
43. Flénet, F.; Kiniry, J.R.; Board, J.E.; Westgate, M.E.; Reicosky, D.C. Row spacing effects on light extinction coefficients of corn, sorghum, soybean, and sunflower. *Agron. J.* **1996**, *88*, 185–190. [CrossRef]
44. Pepper, G.E.; Pearce, R.B.; Mock, J.J. Leaf orientation and yield of maize 1. *Crop Sci.* **1977**, *17*, 883–886. [CrossRef]
45. Srinet, R.; Nandy, S.; Patel, N.R. Estimating leaf area index and light extinction coefficient using Random Forest regression algorithm in a tropical moist deciduous forest, India. *Ecol. Inform.* **2019**, *52*, 94–102. [CrossRef]
46. Baret, F.; de Solan, B.; Lopez-Lozano, R.; Ma, K.; Weiss, M. GAI estimates of row crops from downward looking digital photos taken perpendicular to rows at 57.5 zenith angle: Theoretical considerations based on 3D architecture models and application to wheat crops. *Agric. For. Meteorol.* **2010**, *150*, 1393–1401. [CrossRef]
47. Bréda, N.J. Ground-based measurements of leaf area index: A review of methods, instruments and current controversies. *J. Exp. Bot.* **2003**, *54*, 2403–2417. [CrossRef]
48. Fang, H.; Baret, F.; Plummer, S.; Schaepman-Strub, G. An overview of global leaf area index (LAI): Methods, products, validation, and applications. *Rev. Geophys.* **2019**, *57*, 739–799. [CrossRef]
49. Fournier, R.A.; Hall, R.J. (Eds.) *Hemispherical Photography in Forest Science: Theory, Methods, Applications*; Springer: Dordrecht, The Netherlands, 2017.
50. Welles, J.M.; Norman, J.M. Instrument for indirect measurement of canopy architecture. *Agron. J.* **1991**, *83*, 818–825. [CrossRef]
51. Lang, A.R.G.; Yueqin, X.; Norman, J.M. Crop structure and the penetration of direct sunlight. *Agric. For. Meteorol.* **1985**, *35*, 83–101. [CrossRef]
52. Alignier, A.; Solé-Senan, X.O.; Robleño, I.; Baraibar, B.; Fahrig, L.; Giralt, D.; Gross, N.; Martin, J.; Recasens, J.; Sirami, C.; et al. Configurational crop heterogeneity increases within-field plant diversity. *J. Appl. Ecol.* **2020**, *57*, 654–663. [CrossRef]
53. Moore, I.D.; Norton, T.W.; Williams, J.E. Modelling environmental heterogeneity in forested landscapes. *J. Hydrol.* **1993**, *150*, 717–747. [CrossRef]
54. Lacasa, J.; Hefley, T.J.; Otegui, M.E.; Ciampitti, I.A. A practical guide to estimating the light extinction coefficient with non-linear models—A case study on maize. *Plant Methods* **2021**, *17*, 60. [CrossRef]
55. Lai, G.; Zhang, L.; Liu, Y.; Yi, F.; Zeng, X.; Pan, R. Retrieving leaf area index and extinction coefficient of dominant vegetation canopy in Meijiang Watershed of China using ETM+ data. In Proceedings of the 2012 2nd International Conference on Remote Sensing, Environment and Transportation Engineering, Nanjing, China, 1–3 June 2012; IEEE: Piscataway, NJ, USA, 2012; pp. 1–5.
56. Poblete-Echeverría, C.; Fuentes, S.; Ortega-Farias, S.; Gonzalez-Talice, J.; Yuri, J.A. Digital cover photography for estimating leaf area index (LAI) in apple trees using a variable light extinction coefficient. *Sensors* **2015**, *15*, 2860–2872. [CrossRef] [PubMed]
57. Tan, C.-W.; Zhang, P.-P.; Zhou, X.-X.; Wang, Z.-X.; Xu, Z.-Q.; Mao, W.; Li, W.-X.; Huo, Z.-Y.; Guo, W.-S.; Yun, F. Quantitative monitoring of leaf area index in wheat of different plant types by integrating NDVI and Beer-Lambert law. *Sci. Rep.* **2020**, *10*, 522. [CrossRef]
58. Uchijima, Z. Maize and Rice, Chapter 2. In *Vegetation and the Atmosphere*; Monteith, J.L., Ed.; Academic Press: London, UK, 1976; Volume 2, pp. 33–64. 439p.
59. Zheng, G.; Ma, L.; Eitel, J.U.; He, W.; Magney, T.S.; Moskal, L.M.; Li, M. Retrieving directional gap fraction, extinction coefficient, and effective leaf area index by incorporating scan angle information from discrete aerial lidar data. *IEEE Trans. Geosci. Remote Sens.* **2016**, *55*, 577–590. [CrossRef]
60. De Costa, W.A.J.M.; Dennett, M.D. Is canopy light extinction coefficient a species-specific constant? *Trop. Agric. Res.* **1992**, *4*, 123–137.
61. Costa-Filho, E.; Chávez, J.L.; Zhang, H.; Andales, A.A. An optimized surface aerodynamic temperature approach to estimate maize sensible heat flux and evapotranspiration. *Agric. For. Meteorol.* **2021**, *311*, 108683. [CrossRef]
62. Klopfenstein, T.J.; Erickson, G.E.; Berger, L.L. Maize is a critically important source of food, feed, energy and forage in the USA. *Field Crops Res.* **2013**, *153*, 5–11. [CrossRef]

63. Chung, U.; Gbegbelegbe, S.; Shiferaw, B.; Robertson, R.; Yun, J.I.; Tesfaye, K.; Hoogenboom, G.; Sonder, K. Modeling the effect of a heat wave on maize production in the USA and its implications on food security in the developing world. *Weather Clim. Extrem.* **2014**, *5*, 67–77. [CrossRef]
64. Anderson, M.C.; Neale, C.M.U.; Li, F.; Norman, J.M.; Kustas, W.P.; Jayanthi, H.; Chavez, J.O.S.E. Upscaling ground observations of vegetation water content, canopy height, and leaf area index during SMEX02 using aircraft and Landsat imagery. *Remote Sens. Environ.* **2004**, *92*, 447–464. [CrossRef]
65. Chávez, J.L.; Gowda, P.H.; Howell, T.A.; Neale, C.M.U.; Copeland, K.S. Estimating hourly crop ET using a two-source energy balance model and multispectral airborne imagery. *Irrig. Sci.* **2009**, *28*, 79–91. [CrossRef]
66. Baret, F.; Guyot, G. Potentials and limits of vegetation indices for LAI and APAR assessment. *Remote Sens. Environ.* **1991**, *35*, 161–173. [CrossRef]
67. Clevers, J.G.P.W. Application of a weighted infrared-red vegetation index for estimating leaf area index by correcting for soil moisture. *Remote Sens. Environ.* **1989**, *29*, 25–37. [CrossRef]
68. Gutman, G.; Ignatov, A. The derivation of the green vegetation fraction from NOAA/AVHRR data for use in numerical weather prediction models. *Int. J. Remote Sens.* **1998**, *19*, 1533–1543. [CrossRef]
69. Hatfield, J.L.; Kanemasu, E.T.; Asrar, G.; Jackson, R.D.; Pinter, P.J., Jr.; Reginato, R.J.; Idso, S.B. Leaf-area estimates from spectral measurements over various planting dates of wheat. *Int. J. Remote Sens.* **1985**, *6*, 167–175. [CrossRef]
70. Richardson, A.J.; Wiegand, C.L.; Wanjura, D.F.; Dusek, D.; Steiner, J.L. Multisite analyses of spectral-biophysical data for sorghum. *Remote Sens. Environ.* **1992**, *41*, 71–82. [CrossRef]
71. Gillies, R.R.; Carlson, T.N. Thermal remote sensing of surface soil water content with partial vegetation cover for incorporation into climate models. *J. Appl. Meteorol. Climatol.* **1995**, *34*, 745–756. [CrossRef]
72. Montandon, L.M.; Small, E.E. The impact of soil reflectance on the quantification of the green vegetation fraction from NDVI. *Remote Sens. Environ.* **2008**, *112*, 1835–1845. [CrossRef]
73. Gan, T.Y.; Burges, S.J. Assessment of soil-based and calibrated parameters of the Sacramento model and parameter transferability. *J. Hydrol.* **2006**, *320*, 117–131. [CrossRef]
74. Oleson, K.W.; Emery, W.J.; Maslanik, J.A. Evaluating land surface parameters in the Biosphere-Atmosphere Transfer Scheme using remotely sensed data sets. *J. Geophys. Res. Atmos.* **2000**, *105*, 7275–7293. [CrossRef]
75. Zeng, X.; Dickinson, R.E.; Walker, A.; Shaikh, M.; DeFries, R.S.; Qi, J. Derivation and evaluation of global 1-km fractional vegetation cover data for land modeling. *J. Appl. Meteorol.* **2000**, *39*, 826–839. [CrossRef]
76. Long, D.; Singh, V.P. A two-source trapezoid model for evapotranspiration (TTME) from satellite imagery. *Remote Sens. Environ.* **2012**, *121*, 370–388. [CrossRef]
77. Monteith, J.L. *Principles of Environmental Physics*; Edward Arnold: London, UK, 1975.
78. Campbell, G.S. Plants and Their Environment. In *An Introduction to Environmental Biophysics*; Springer: New York, NY, USA, 1977; pp. 115–126.
79. Campbell, G.S. Derivation of an angle density function for canopies with ellipsoidal leaf angle distributions. *Agric. For. Meteorol.* **1990**, *49*, 173–176. [CrossRef]
80. Campbell, G.S.; Van Evert, F.K. Light interception by plant canopies: Efficiency and architecture. *Resour. Capture Crops* **1994**, *52*, 35.
81. Peel, M.C.; Finlayson, B.L.; McMahon, T.A. Updated world map of the Köppen-Geiger climate classification. *Hydrol. Earth Syst. Sci.* **2007**, *11*, 1633–1644. [CrossRef]
82. Allen, R.G.; Pereira, L.S.; Raes, D.; Smith, M. *Crop Evapotranspiration-Guidelines for Computing Crop Water Requirements-FAO Irrigation and Drainage Paper 56*; FAO: Rome, Italy, 1998; Volume 300, p. D05109.
83. ASCE-EWRI. *The ASCE Standardized Reference Evapotranspiration Equation*; Report 0-7844-0805-X, ASCE Task Committee on Standardization of Reference Evapotranspiration; The American Society of Civil Engineers: Reston, VA, USA, 2005.
84. Garcia, L.A.; Elhaddad, A.; Altenhofen, J.; Hattendorf, M. Developing corn regional crop coefficients using a satellite-based energy balance model (ReSET-Raster) in the South Platte River Basin of Colorado. *J. Irrig. Drain. Eng.* **2013**, *139*, 821–832. [CrossRef]
85. Roy, D.P.; Wulder, M.A.; Loveland, T.R.; Woodcock, C.E.; Allen, R.G.; Anderson, M.C.; Helder, D.; Irons, J.R.; Johnson, D.M.; Kennedy, R.; et al. Landsat-8: Science and product vision for terrestrial global change research. *Remote Sens. Environ.* **2014**, *145*, 154–172. [CrossRef]
86. Vermote, E.; Justice, C.; Claverie, M.; Franch, B. Preliminary analysis of the performance of the Landsat 8/OLI land surface reflectance product. *Remote Sens. Environ.* **2016**, *185*, 46–56. [CrossRef]
87. Main-Knorn, M.; Pflug, B.; Louis, J.; Debaecker, V.; Müller-Wilm, U.; Gascon, F. Sen2Cor for sentinel-2. In Proceedings of the Image and Signal Processing for Remote Sensing XXIII, Warsaw, Poland, 11–14 September 2017; SPIE: Bellingham, WA, USA, 2017; Volume 10427, pp. 37–48.
88. Su, W.; Zhang, M.; Jiang, K.; Zhu, D.; Huang, J.; Wang, P. Atmospheric correction method for Sentinel-2 satellite imagery. *Acta Opt. Sin.* **2018**, *38*, 0128001. [CrossRef]
89. Planet Team. *Planet Application Program Interface: In Space for Life on Earth*; Planet Team: San Francisco, CA, USA, 2017; Available online: https://api.planet.com (accessed on 15 December 2023).
90. Csillik, O.; Belgiu, M.; Asner, G.P.; Kelly, M. Object-Based Time-Constrained Dynamic Time Warping Classification of Crops Using Sentinel-2. *Remote Sens.* **2019**, *11*, 1257. [CrossRef]

91. Kington, J.D., IV; Jordahl, K.A.; Kanwar, A.N.; Kapadia, A.; Schönert, M.; Wurster, K. Spatially and Temporally Consistent Smallsat-Derived Basemaps for Analytic Applications. In Proceedings of the AGU Fall Meeting Abstracts, San Francisco, CA, USA, 16 December 2019; Volume 2019, p. IN13B-0716.
92. Li, X.; Zhu, W.; Xie, Z.; Zhan, P.; Huang, X.; Sun, L.; Duan, Z. Assessing the Effects of Time Interpolation of NDVI Composites on Phenology Trend Estimation. *Remote Sens.* **2021**, *13*, 5018. [CrossRef]
93. Vorobiova, N.; Chernov, A. Curve fitting of MODIS NDVI time series in the task of early crops identification by satellite images. *Procedia Eng.* **2017**, *201*, 184–195. [CrossRef]
94. Sobol, I.M. Global sensitivity indices for non-linear mathematical models and their Monte Carlo estimates. *Math. Comput. Simul.* **2001**, *55*, 271–280. [CrossRef]
95. Sobol', I.Y.M. On sensitivity estimation for non-linear mathematical models. *Mat. Model.* **1990**, *2*, 112–118.
96. Cannavó, F. Sensitivity analysis for volcanic source modeling quality assessment and model selection. *Comput. Geosci.* **2012**, *44*, 52–59. [CrossRef]